The Astrophysical Journal Supplement Series, 278:59 (17pp), 2025 June https://doi.org/10.3847/1538-4365/add0b1

SIP-IFVM: A Time-evolving Coronal Model with an Extended Magnetic Field Decomposition Strategy

Haopeng Wang[1], Liping Yang[2], Stefaan Poedts[1,3], Andrea Lani[1,4], Yuhao Zhou[1], Yuhang Gao[1,5], Luis Linan[1], Jiakun Lv[6], Tinatin Baratashvili[1], Jinhan Guo[1,7], Rong Lin[1,5], Zhan Su[2,8], Caixia Li[9], Man Zhang[2], Wenwen Wei[10], Yun Yang[11], Yucong Li[1,2,8], Xinyi Ma[2,8], Edin Husidic[1,12], Hyun-Jin Jeong[1,13], Mahdi Najafi-Ziyazi[1], Juan Wang[14], and Brigitte Schmieder[1,15,16]

[1] Centre for Mathematical Plasma-Astrophysics, Department of Mathematics, KU Leuven, Celestijnenlaan 200B, 3001 Leuven, Belgium; haopeng.wang1@kuleuven.be
[2] SIGMA Weather Group, State Key Laboratory of Space Weather, National Space Science Center, Chinese Academy of Sciences, Beijing 100190, People's Republic of China; lpyang@swl.ac.cn
[3] Institute of Physics, University of Maria Curie-Skłodowska, ul. Radziszewskiego 10, 20-031 Lublin, Poland
[4] Von Karman Institute for Fluid Dynamics, Waterloosesteenweg 72, 1640 Sint-Genesius-Rode, Brussels, Belgium
[5] School of Earth and Space Sciences, Peking University, Beijing 100871, People's Republic of China
[6] Beijing Institute of Applied Meteorology, Beijing 100029, People's Republic of China
[7] School of Astronomy and Space Science and Key Laboratory of Modern Astronomy and Astrophysics, Nanjing University, Nanjing 210023, People's Republic of China
[8] College of Earth and Planetary Sciences, University of Chinese Academy of Sciences, Beijing 100049, People's Republic of China
[9] Shenzhen Key Laboratory of Ultraintense Laser and Advanced Material Technology, Center for Intense Laser Application Technology, and College of Engineering Physics, Shenzhen Technology University, Shenzhen 518118, People's Republic of China
[10] Space Sciences Laboratory, University of California, Berkeley, CA 94720, USA
[11] School of Mathematical Sciences, Ministry of Education Key Laboratory for NSLSCS, Nanjing Normal University, Nanjing 210023, People's Republic of China
[12] Department of Physics and Astronomy, University of Turku, 20014 Turku, Finland
[13] School of Space Research, Kyung Hee University, Yongin, 17104, Republic of Korea
[14] School of Systems Science, Beijing Normal University, Beijing 100875, People's Republic of China
[15] Observatoire de Paris, LIRA, UMR8254 (CNRS), F-92195 Meudon Principal Cedex, France
[16] SUPA, School of Physics & Astronomy, University of Glasgow, Glasgow G12 8QQ, UK
Received 2025 March 17; revised 2025 April 21; accepted 2025 April 24; published 2025 June 10

Abstract

Time-evolving magnetohydrodynamic (MHD) coronal modeling, driven by a series of time-dependent photospheric magnetograms, represents a new generation of coronal simulations. This approach offers more realistic results than traditional steady coronal models constrained by a static magnetogram. However, its practical application is significantly limited by the low computational efficiency and poor numerical stability in solving low-β issues common in coronal simulations. To address this, we propose an extended magnetic field decomposition strategy and successfully implement it in an implicit MHD coronal model. The traditional decomposition strategies split the magnetic field into a time-invariant potential field and a time-dependent component $\boldsymbol{B}_1$. This works well for quasi-steady-state coronal simulations where $|\boldsymbol{B}_1|$ is typically small. However, when the inner-boundary magnetic field evolves, $|\boldsymbol{B}_1|$ can grow significantly, and its discretization errors often lead to nonphysical negative thermal pressure, ultimately causing the simulation to crash. In the extended magnetic field decomposition strategy, we split the magnetic field into a temporally piecewise-constant field and a time-varying component, $\boldsymbol{B}_1$. This effectively keeps $|\boldsymbol{B}_1|$ consistently small throughout the simulations and performs well in solving time-evolving low-β issues, thereby outperforming traditional methods. We incorporate this improved strategy into our implicit MHD coronal model and apply it to simulate the evolution of coronal structures within 0.1 au over two solar-maximum Carrington rotations. The results show that this coronal model effectively captures observational features and performs more than 80 times faster than real-time evolutions using only 192 CPU cores, making it well suited for practical applications in simulating the time-evolving corona.

Unified Astronomy Thesaurus concepts: The Sun (1693); Magnetohydrodynamics (1964); Magnetohydrodynamical simulations (1966); Solar corona (1483)

Materials only available in the online version of record: animation

1. Introduction

Space weather can impact the performance and reliability of both space-borne and ground-based technological systems and pose risks to human health. To enable timely action in mitigating damage from severe space weather events, advanced Sun-to-Earth model chains should be developed (e.g., X. S. Feng et al. 2011, 2013; J. Pomoell & S. Poedts 2018; S. Poedts et al. 2020; K. Hayashi et al. 2021) to better understand space weather mechanisms and provide reliable forecasts hours to days in advance (e.g., D. N. Baker 1998; X. S. Feng et al. 2013; H. E. J. Koskinen et al. 2017; X. S. Feng 2020). In the Sun-to-Earth modeling chain, observed photospheric magnetic fields serve as input for the solar coronal model, providing inner boundary conditions for the inner heliospheric model, which then supplies boundary

information to the geomagnetic model. The coronal model is essential for initializing other models and is key in accurately simulating solar disturbances such as coronal mass ejections (CMEs; M. Brchnelova et al. 2022; B. Kuźma et al. 2023; B. Perri et al. 2023). However, physics-based MHD coronal models are also the most complex and computationally intensive component (H. P. Wang et al. 2025a, 2025b), and sometimes encounter problems with low β (the ratio of the thermal pressure to the magnetic pressure), where β can drop as low as 10^{-4} near the solar surface (P.-A. Bourdin 2017), leading to severe challenges to stability and efficiency (X. S. Feng et al. 2021; H. P. Wang et al. 2022a).

In most MHD coronal simulations, time steps are limited to a few seconds due to the restriction of the Courant–Friedrichs–Lewy (CFL) stability condition. Consequently, depending on the mesh resolution, even state-of-the-art quasi-steady-state coronal simulations require 10,000–100,000 CPU-hours to reach a quasi-steady state (X. S. Feng et al. 2019; V. Réville et al. 2020). In contrast, for most MHD inner heliospheric models, the CFL-limited time steps are typically of the order of 10 minutes (T. Detman et al. 2006; K. Hayashi 2012). As a result, coronal models require significantly greater computational resources to remain synchronized with inner heliospheric models. Although empirical solar coronal models (C. N. Arge et al. 2003) offer higher efficiency, they discard important information and fail to deliver the necessary accuracy in forecasts (E. Samara et al. 2021). Therefore, further efforts are needed to develop more efficient and accurate MHD coronal models. Implicit temporal discretization strategies can help overcome the limitations imposed by the CFL condition, thereby enhancing computational efficiency by allowing longer time steps.

Recently, several successful attempts have been made to increase the efficiency of MHD coronal models by using implicit solvers (B. Perri et al. 2018, 2022, 2023; Y. Wang et al. 2019; X. S. Feng et al. 2021; H. P. Wang et al. 2022a, 2022b, 2025a; B. Kuźma et al. 2023). In the implicit algorithm, the convergence rate is improved by selecting a considerable time step. Additionally, both the second-order backward differentiation formula (BDF2) with Newton iterations at each time step and the pseudo–time marching method, which introduces a pseudotime at each physical time step, are employed to improve temporal accuracy in implicit coronal models (J. H. Guo et al. 2023; L. Linan et al. 2023; H. P. Wang et al. 2025a). While these models have achieved the desired speedup, they remain constrained by a time-invariant magnetogram, which contrasts with the reality that the solar coronal structure evolves (M. J. Owens et al. 2017). This discrepancy leads to differences between simulation results and coronal observations (M. D. Cash et al. 2015; V. Réville et al. 2020).

Many researchers have focused on developing time-evolving coronal models to address the limitations of commonly used quasi-steady-state coronal models, which do not account for the evolution of coronal structures. These models, typically driven by hundreds of time-varying observed photospheric magnetograms, can capture the evolution of coronal structures with higher fidelity (L. P. Yang et al. 2012; A. Yeates et al. 2018; X. S. Feng et al. 2023). They may also improve the realism and reliability of solar wind and CME modeling (R. Lionello et al. 2023). However, time-evolving MHD coronal simulations remain prohibitively computationally expensive (A. Yeates et al. 2018). One of the main reasons is that most state-of-the-art time-evolving coronal models (L. P. Yang et al. 2012; K. Hayashi et al. 2021; R. Lionello et al. 2023) still rely on explicit or semi-implicit approaches, where only specific source terms are treated implicitly while the time step remains constrained by the explicitly treated terms, leading to extremely low efficiency. As a result, explicit or semi-implicit MHD coronal simulations typically require thousands of computing cores to achieve faster-than-real-time execution. A more detailed description of time-evolving coronal models is given by H. P. Wang et al. (2025b).

Furthermore, H. P. Wang et al. (2025b) extended the quasi-steady-state Coolfluid Coronal Unstructured (COCONUT) model, a novel implicit MHD solar corona model based on the Computational Object-Oriented Libraries for Fluid Dynamics (COOLFluiD; D. Kimpe et al. 2005; A. Lani et al. 2005, 2013),[17] into a time-evolving coronal model. It is the first fully implicit time-evolving MHD coronal model, allowing for long time steps exceeding the CFL condition. It can simulate the evolution of a full Carrington rotation (CR) period in just 9 hr of computational time (with a time step of 10 minutes using 1080 CPU cores and approximately 1.5 million cells). However, it currently struggles with resolving low-β issues. Given that $(\boldsymbol{B}+\epsilon\boldsymbol{B})^2-\boldsymbol{B}^2\equiv 2\epsilon\boldsymbol{B}^2+\epsilon^2\boldsymbol{B}^2$, where $\epsilon\boldsymbol{B}$ represents the magnetic field discretization error, the magnetic pressure discretization error can be comparable to thermal pressure in low-β regions. This can lead to nonphysical negative thermal pressure when deriving thermal pressure from energy density. Reducing magnetic field discretization errors is crucial to mitigating these issues.

By solving decomposed MHD equations, where the magnetic field $\boldsymbol{B}$ is split into a time-dependent field $\boldsymbol{B}_1$ and a time-independent potential (e.g., T. Tanaka 1995; K. G. Powell et al. 1999; F. G. Fuchs et al. 2010; X. C. Guo 2015) or even an arbitrary background magnetic field $\boldsymbol{B}_0$ (C. Xia et al. 2018), some previous works (e.g., X. S. Feng et al. 2010, 2021; C. X. Li et al. 2018; Y. Wang et al. 2019; H. P. Wang et al. 2022a, 2022b, 2025a) have reduced magnetic field discretization errors and significantly improved the numerical stability of quasi-steady-state MHD coronal modeling. However, as $|\boldsymbol{B}_1|$ increases in the time-evolving coronal simulations and does not satisfy homogeneous boundary conditions anymore, discretization errors in $\boldsymbol{B}_1$ are still likely to result in nonphysical negative thermal pressure and cause the code to break down. Therefore, L. Griton (2018) incorporated the rotation of the potential magnetic field $\boldsymbol{B}_0$ in simulations of planetary magnetospheres, treating $\boldsymbol{B}_0$ as a time-dependent field that corotates with the planet. This approach helps keep $|\boldsymbol{B}_1|$ small and satisfies homogeneous boundary conditions throughout the simulations, thus improving the numerical stability of the MHD planetary magnetospheric code. Given that time-evolving coronal simulations involve not only differential rotation but also magnetic flux emergence and cancellation, we further introduce a temporally piecewise-constant variable in this paper to accommodate part of the nonpotential field, ensuring that $|\boldsymbol{B}_1|$ remains consistently small throughout the simulations of the time-evolving corona.

Based on the above considerations, the paper is organized as follows. In Section 2, we introduce the numerical formulation and implementations of the time-evolving MHD coronal model. The governing equations, the derivation of the

[17] https://github.com/andrealani/COOLFluiD/wiki

extended magnetic field decomposition strategy, the processing of time-evolving boundary conditions, and the positivity-preserving (PP) measures applied to enhance the model's numerical stability are described in detail. In Section 3, we present the simulation results, including the evolution of the corona during CRs 2110 and 2111, and a comparison between the time-evolving simulation results and observational data. Finally, in Section 4, we summarize the key features of the efficient and numerically stable fully implicit time-evolving coronal model and offer concluding remarks.

2. Governing Equations and Numerical Methods

2.1. The Governing Equations

This time-evolving MHD global coronal model is based on the time-accurate Solar Interplanetary Phenomena Implicit Finite Volume Method (SIP-IFVM) coronal model (H. P. Wang et al. 2025a). Additionally, we incorporate the optically thin radiative loss and adjust the adiabatic index γ from 1.05 to 5/3 to better represent the adiabatic process. Furthermore, we develop an extended magnetic field decomposition strategy, the derivation of which is available in Section 2.5, and employ it to enhance the numerical stability of the time-evolving thermodynamic MHD coronal model. The governing equations are described as follows:

$$\begin{cases} \frac{\partial \rho}{\partial t} + \nabla \cdot (\rho \boldsymbol{v}) = 0 \\ \frac{\partial (\rho \boldsymbol{v})}{\partial t} + \nabla \cdot \left[\rho \boldsymbol{v}\boldsymbol{v} + \left(p + \frac{\boldsymbol{B}^2}{2} - \frac{\boldsymbol{B}_{00}^2}{2} \right) \boldsymbol{I} - \boldsymbol{B}\boldsymbol{B} + \boldsymbol{B}_{00}\boldsymbol{B}_{00} \right] \\ \quad = -\nabla \cdot (\boldsymbol{B}_1 + \boldsymbol{B}_{01})\boldsymbol{B} - \frac{\rho G M_s}{r^3}\boldsymbol{r} + \boldsymbol{S}_m \\ \frac{\partial E_1}{\partial t} + \nabla \cdot [(E_1 + p_{T1} + \boldsymbol{B}_1 \cdot \boldsymbol{B}_0)\boldsymbol{v} - \boldsymbol{B}(\boldsymbol{v} \cdot \boldsymbol{B}_1)] = -\boldsymbol{B}_1 \cdot \frac{\partial \boldsymbol{B}_0}{\partial t} - \nabla \cdot (\boldsymbol{B}_1 + \boldsymbol{B}_{01})(\boldsymbol{v} \cdot \boldsymbol{B}_1) \\ \quad -\boldsymbol{v} \cdot \nabla(\boldsymbol{B}_0 \cdot \boldsymbol{B}) + (\boldsymbol{v} \cdot \nabla \boldsymbol{B}) \cdot \boldsymbol{B}_0 + \boldsymbol{B} \cdot \nabla(\boldsymbol{B}_0 \cdot \boldsymbol{v}) - (\boldsymbol{B} \cdot \nabla \boldsymbol{v}) \cdot \boldsymbol{B}_0 - \rho \boldsymbol{v} \cdot \boldsymbol{r} \frac{G M_s}{r^3} + S_E \\ \frac{\partial \boldsymbol{B}_1}{\partial t} + \nabla \cdot (\boldsymbol{v}\boldsymbol{B} - \boldsymbol{B}\boldsymbol{v}) = -\frac{\partial \boldsymbol{B}_{01}}{\partial t} - \nabla \cdot (\boldsymbol{B}_1 + \boldsymbol{B}_{01})\boldsymbol{v}, \end{cases} \tag{1}$$

where $\boldsymbol{B} = (B_x, B_y, B_z)^T$ and $\boldsymbol{v} = (u, v, w)^T$ denote the magnetic field and velocity in a Cartesian coordinate system, respectively, ρ is the plasma density, $\boldsymbol{B}_{00} = (B_{00x}, B_{00y}, B_{00z})^T$ is a static potential field, $\boldsymbol{B}_{01} = (B_{01x}, B_{01y}, B_{01z})^T$ is a temporally piecewise-constant field and $\boldsymbol{B}_0 = \boldsymbol{B}_{00} + \boldsymbol{B}_{01}$, $\boldsymbol{B}_1 = \boldsymbol{B} - \boldsymbol{B}_0$, $E_1 = \frac{p}{\gamma - 1} + \frac{1}{2}\rho \boldsymbol{v}^2 + \frac{1}{2}\boldsymbol{B}_1^2$ with the adiabatic index $\gamma = 5/3$, and $p_{T1} = p + \frac{\boldsymbol{B}_1^2}{2}$. During the simulations, as detailed in Section 2.5, when $\frac{p}{0.5\,\boldsymbol{B}_1^2}$ falls below a specific threshold, we update $\boldsymbol{B}_{01}$, $\boldsymbol{B}_1$, and E_1 to $\boldsymbol{B}_{01} + \boldsymbol{B}_1$, $\boldsymbol{0}$, and $\frac{p}{\gamma - 1} + \frac{1}{2}\rho \mathbf{v}^2$, respectively. We then solve Equation (1) with $\frac{\partial \boldsymbol{B}_{01}}{\partial t} = 0$ to advance the solution in time. This process continues until $\frac{p}{0.5\,\boldsymbol{B}_1^2}$ again falls below the threshold, at which point we repeat the procedure. In the definition of the magnetic field, a factor of $\frac{1}{\sqrt{\mu_0}}$ is absorbed, with $\mu_0 = 4 \times 10^{-7}\pi\,\mathrm{H\,m^{-1}}$ denoting the magnetic permeability. Additionally, G is the universal gravitational constant, M_s denotes the mass of the Sun, and $GM_s = 1.327927 \times 10^{20}\,\mathrm{m^3\,s^{-2}}$. The thermal pressure of the plasma is defined as $p = \Re \rho T$, where $\Re = 1.653 \times 10^4\,\mathrm{m^2\,s^{-2}\,K^{-1}}$ denotes the gas constant, and T is the temperature of the bulk plasma. In addition, $\boldsymbol{r}$ is the position vector and $r = |\boldsymbol{r}|$ refers to the heliocentric distance. $S_E = Q_e + \boldsymbol{v} \cdot \boldsymbol{S}_m + \nabla \cdot \boldsymbol{q} + Q_{\mathrm{rad}}$ is the energy source term, where Q_e and $\boldsymbol{S}_m$, defined the same as by X. S. Feng et al. (2021) and H. P. Wang et al. (2022a, 2022b), are used to mimic the effect of coronal heating and solar wind acceleration. Additionally, Q_{rad} and $\nabla \cdot \boldsymbol{q}$ represent radiation loss and thermal conduction, respectively.

By assuming the radiative losses to be optically thin (R. Rosner et al. 1978; Y. H. Zhou et al. 2021), the radiative term Q_{rad} is defined as

$$Q_{\mathrm{rad}} = -n_e n_p \Lambda(T), \tag{2}$$

where the proton number density n_p is assumed to be equal to the electron number density n_e for the hydrogen plasma. Similar to B. van der Holst et al. (2014) and H. P. Wang et al. (2025a), the radiative cooling function $\Lambda(T)$ in this paper is derived from version 10 of CHIANTI (K. P. Dere et al. 1997, 2023), an atomic database for emission lines. As done by C. Xia et al. (2011) and H. P. Wang et al. (2025a), we set $\Lambda(T)$ to zero when $T < 2 \times 10^4$ K. The heat flux $\boldsymbol{q}$ is defined in a Spitzer form or collisionless form, mainly according to the radial distance (J. V. Hollweg 1978):

$$\boldsymbol{q} = \begin{cases} \xi T^{5/2}(\hat{\boldsymbol{b}} \cdot \nabla T)\hat{\boldsymbol{b}} & \text{if } 1\,R_s \leqslant r \leqslant 10\,R_s \\ -\alpha n_e k_{\mathrm{B}} T \boldsymbol{v} & \text{if } r > 10\,R_s, \end{cases} \tag{3}$$

where $\hat{\boldsymbol{b}} = \frac{\boldsymbol{B}}{|\boldsymbol{B}|}$, $\xi = 9 \times 10^{-12}\,\mathrm{J\,m^{-1}\,s^{-1}\,K^{-7/2}}$ (E. Endeve et al. 2003; X. S. Feng et al. 2010), the parameter α is set to 3/2 (E. Endeve et al. 2003), n_e is the electron number density, and $k_{\mathrm{B}} = 1.380649 \times 10^{-23}\,\mathrm{J\,K^{-1}}$ is the Boltzmann constant. The Spitzer form of heat flux is defined along the magnetic field, whereas the collisionless form is defined along the velocity vector. To ensure a smooth transition between these two forms, we hybridize the Spitzer form $\boldsymbol{q}_{\mathrm{Spitzer}}$ and collisionless form $\boldsymbol{q}_{\mathrm{Collisionless}}$ based on the Alfvénic Mach number over the domain $1\ R_s \leqslant r \leqslant 10\ R_s$, as described in Equation (4):

$$\boldsymbol{q} = \min\left(1, \frac{V_a}{|\boldsymbol{v}|}\right)\boldsymbol{q}_{\mathrm{Spitzer}} + \left(1 - \min\left(1, \frac{V_a}{|\boldsymbol{v}|}\right)\right) \times \boldsymbol{q}_{\mathrm{Collisionless}}, \ \text{if}\, 1\,R_s \leqslant r \leqslant 10\,R_s, \tag{4}$$

where $V_a = \frac{|\boldsymbol{B}|}{\rho^{0.5}}$ is the Alfvén speed. Meanwhile, we apply a linear smoothing transition (Z. Mikić et al. 1999; R. Lionello et al. 2008) between Equation (4) and $\boldsymbol{q}_{\rm Collisionless}$ over the domain of $7.5\,R_s \leqslant r \leqslant 10\,R_s$. In our time-evolving coronal simulation, the plasma velocity occasionally reaches extraordinarily high values, exceeding $1000\,{\rm km\,s^{-1}}$, near low-β regions. Therefore, we enhance the heat conduction efficiency in low-β regions and ultimately adopt the following plasma β-dependent heat flux $\boldsymbol{q}^*$:

$$\boldsymbol{q}^* = \boldsymbol{q}\left(1 + \tanh\left(\frac{1}{\beta} \times \frac{1}{100}\right)\right). \tag{5}$$

2.2. Spatial Discretization

We adopt Godunov's method to advance cell-averaged solutions in time by solving a Riemann problem at each cell interface (S. K. Godunov 1959; B. Einfeldt et al. 1991). The computational domain is a spherical shell ranging from 1 R_s to 20 R_s. The six-component composite mesh (X. S. Feng et al. 2010; X. S. Feng 2020; H. P. Wang et al. 2022a, 2025a) with each identical component being a low-latitude spherical mesh confined by $\left(\frac{\pi}{4} - \delta_\theta \leqslant \theta \leqslant \frac{3\pi}{4} + \delta_\theta\right) \times \left(\frac{3\phi}{4} - \delta_\phi \leqslant \phi \leqslant \frac{5\pi}{4} + \delta_\phi\right)$ and discretized to $96 \times 42 \times 42$ grid cells, is adopted. Here, δ_θ and δ_ϕ are adjustable parameters proportionally dependent on the grid spacing entailed for the minimum overlapping area.

As usual, the following discretized integral equations are obtained by integrating Equation (1) over the hexahedral cell i and applying Gauss's theorem to convert the volume integral of the flux divergence into a surface integral:

$$V_i \frac{\partial \boldsymbol{U}_i}{\partial t} + \boldsymbol{R}_i = \boldsymbol{0}, \tag{6}$$

where $\boldsymbol{R}_i = \oint_{\partial V_i} \boldsymbol{F} \cdot \boldsymbol{n} d\Gamma - V_i \boldsymbol{S}_i$ denotes the residual operator over cell i. Here, $\oint_{\partial V_i} \boldsymbol{F} \cdot \boldsymbol{n} d\Gamma = \sum_{j=1}^{6} \boldsymbol{F}_{ij}(\boldsymbol{U}_L, \boldsymbol{U}_R) \cdot \boldsymbol{n}_{ij} \Gamma_{ij}$; $\boldsymbol{S}_i = \boldsymbol{S}_{{\rm Powell},i} + \boldsymbol{S}_{{\rm gra},i} + \boldsymbol{S}_{{\rm heat},i}$ corresponds to the Godunov–Powell source terms, the gravitational force, and the heating and radiation loss source terms in cell i, respectively. $\boldsymbol{U}_i$ denotes the cell-averaged solution variables in cell i. As described in Section 2.5, when $\min_{\forall {\rm cell}_i} \frac{p_i}{0.5\,\boldsymbol{B}_{1,i}^2}$ drops below a threshold, in this paper we adopt 10, we update $\boldsymbol{B}_{01,i}$, $\boldsymbol{B}_{1,i}$, and $E_{1,i}$ to $\boldsymbol{B}_{01,i} + \boldsymbol{B}_{1,i}$, $\boldsymbol{0}$, and $\frac{p_i}{\gamma - 1} + \frac{1}{2}\rho_i \boldsymbol{v}_i^2$, respectively.

Additionally, in Equation (6), V_i is the volume of cell i, Γ_{ij} is the area of interface shared by cell i and its neighboring cell j, and $\boldsymbol{n}_{ij}$ is the unit normal vector of Γ_{ij}, pointing from cell i to cell j. Following the approach of X. S. Feng et al. (2021) and H. P. Wang et al. (2022a), the cell-averaged Powell source term is calculated as

$$\begin{aligned}\boldsymbol{S}_{{\rm Powell},i} = \frac{1}{V_i}\sum_{j=1}^{6} \boldsymbol{T}_{8ij}^{-1} \boldsymbol{Q}(\boldsymbol{U}_{nL})(B_{1nL} + B_{01nL} - B_{1n,i} \\ - B_{01n,i} - \eta(B_{1nR} + B_{01nR} - B_{1nL} - B_{01nL}))\Gamma_{ij},\end{aligned} \tag{7}$$

where $\eta = \frac{S_L}{S_R - S_L}$ (K. L. Wu & C. W. Shu 2019), $\boldsymbol{T}_{8ij} = \begin{pmatrix} 1 & \boldsymbol{0} & 0 & \boldsymbol{0} \\ \boldsymbol{0} & \boldsymbol{T}_{ij} & \boldsymbol{0} & \boldsymbol{0} \\ 0 & \boldsymbol{0} & 1 & \boldsymbol{0} \\ \boldsymbol{0} & \boldsymbol{0} & \boldsymbol{0} & \boldsymbol{T}_{ij} \end{pmatrix}$, and $\boldsymbol{T}_{ij} = \left(\boldsymbol{n}_{ij}, \boldsymbol{t}_{1ij}, \boldsymbol{t}_{2ij}\right)^T$ is a rotation matrix that transforms the (x, y, z) coordinate system to the (n, t_1, t_2) coordinate system. Here, $\boldsymbol{t}_{1ij}$ and $\boldsymbol{t}_{2ij}$ are two unit orthogonal tangential vectors of cell face Γ_{ij} (e.g., X. S. Feng 2020, and references therein), S_L and S_R are the velocities of two fast waves as defined by H. P. Wang et al. (2022a), and $\boldsymbol{Q}(\boldsymbol{U}_{nL}) = (0, -\boldsymbol{T}_{ij} \cdot \boldsymbol{B}_{i,L}, -\boldsymbol{v}_{i,L} \cdot \boldsymbol{B}_{1i,L}, -\boldsymbol{T}_{ij} \cdot \boldsymbol{v}_{i,L})^T$. The subscripts "$_i$," "$_L$," and "$_R$" denote the corresponding variables at the centroid of cell i, and on Γ_{ij} extrapolated from cell i and from cell j, respectively. Moreover, $\boldsymbol{S}_{{\rm gra},i}$ and $Q_{{\rm rad},i}$ included in $\boldsymbol{S}_{{\rm heat},i}$ are defined by evaluating their respective formulations using the corresponding variables at the centroid of cell i. The inviscid flux through the interface Γ_{ij}, described as $\boldsymbol{F}_{ij}(\boldsymbol{U}_L, \boldsymbol{U}_R) \cdot \boldsymbol{n}_{ij}$, is computed using the positive-preserving (PP) Harten–Lax–van Leer (HLL) Riemann solver (X. S. Feng et al. 2021), equipped with a self-adjustable dissipation term (H. P. Wang et al. 2025b). The cell-averaged heat conduction term $(\nabla \cdot \boldsymbol{q})_i$ is calculated following Gauss's theorem, as described by H. P. Wang et al. (2022a). The volume heating coefficients in $Q_{e,i}$ and $\boldsymbol{S}_{m,i}$ are precomputed from six-hourly updated magnetograms and are stored as a time series and then linearly interpolated to the current time step during the time-evolving coronal simulations.

Following H. P. Wang et al. (2025a), the second-order PP reconstruction method is used to reconstruct the piecewise polynomials of primitive variables $\{\rho, u, v, w, p, T\}$ on the cell surface Γ_{ij},

$$\begin{aligned}X_i(\boldsymbol{x}) = X|_i + \Psi_i \nabla X|_i \cdot (\boldsymbol{x} - \boldsymbol{x}_i), \\ X \in \{\rho,\ u,\ v,\ w,\ p,\ T\},\end{aligned} \tag{8}$$

where $X|_i$ is the corresponding variable at $\boldsymbol{x}_i$ (the centroid of cell i), $\nabla X|_i = \left(\frac{\partial X}{\partial x}, \frac{\partial X}{\partial y}, \frac{\partial X}{\partial z}\right)\Big|_i$ is the derivative of X at $\boldsymbol{x}_i$, and Ψ_i is the limiter used to control spatial oscillation. Furthermore, a globally solenoidality-preserving approach (X. S. Feng et al. 2019, 2021) is employed to enforce the divergence-free constraint for the magnetic field. Considering that reducing the magnetic field discretization error is crucial for enhancing the PP property of MHD models in low-β regions (H. P. Wang et al. 2025a), and given that the MHD decomposition method introduced in this paper has improved the numerical stability of our code, we opt to abandon the limiter as follows in the calculation of the piecewise polynomial representations for $\boldsymbol{B}_{00}(\boldsymbol{x})$, $\boldsymbol{B}_0(\boldsymbol{x})$, and $\boldsymbol{B}_1(\boldsymbol{x})$ to minimize discretization error in the magnetic field:

$$\begin{aligned}X_i(\boldsymbol{x}) = X|_i + \nabla X|_i \cdot (\boldsymbol{x} - \boldsymbol{x}_i), \\ X \in \{\boldsymbol{B}_{00x},\ \boldsymbol{B}_{00y},\ \boldsymbol{B}_{00z},\ \boldsymbol{B}_{0x},\ \boldsymbol{B}_{0y},\ \boldsymbol{B}_{0z},\ \boldsymbol{B}_{1x},\ \boldsymbol{B}_{1y},\ \boldsymbol{B}_{1z}\}.\end{aligned} \tag{9}$$

2.3. Temporal Integration

In this paper, we first apply the following backward Euler temporal integration to Equation (6) to perform a quasi-steady-

state coronal simulation constrained by one time-invariant magnetogram (X. S. Feng et al. 2021; H. P. Wang et al. 2022a):

$$V_i \frac{\Delta \boldsymbol{U}_i^n}{\Delta t} + \boldsymbol{R}_i^{n+1} = \boldsymbol{0}. \tag{10}$$

The superscripts "n" and "$n+1$" denote the time level, $\Delta \boldsymbol{U}_i^n = \boldsymbol{U}_i^{n+1} - \boldsymbol{U}_i^n$ is the solution increment between the nth and $(n+1)$th time levels, and $\Delta t = t^{n+1} - t^n$ is the time increment. Subsequently, we evolve the magnetograms to carry out the time-evolving coronal simulation, enabling us to capture the temporal evolution of coronal structures. To improve the temporal accuracy for time-evolving simulations, we further employ the pseudo–time marching method (H. P. Wang et al. 2025a), which introduced a pseudotime τ to Equation (10) and updated the solution during each physical time step Δt by solving a steady-state problem on τ, to solve Equation (10):

$$V_i \frac{\Delta \boldsymbol{U}_i}{\Delta \tau} + \left(V_i \frac{\Delta \boldsymbol{U}_i^n}{\Delta t} + \boldsymbol{R}_i^{n+1} \right) = \boldsymbol{0}. \tag{11}$$

Here, $\Delta\tau$ is a pseudo–time step, and $\Delta \boldsymbol{U}_i$ is the solution increment during $\Delta\tau$.

Similar to the PP measure employed by H. P. Wang et al. (2025b), we make the following adjustment on the updated density and thermal pressure during each pseudotime iteration in the domain of $1\,R_s \leqslant r \leqslant 2\,R_s$:

$$\begin{cases} \rho_i = \Upsilon_{\rho_i} \dfrac{\boldsymbol{B}_i^2}{V_{A,\max}^2} + (1 - \Upsilon_{\rho_i}) \rho_{o,i} \\ p_i = \Upsilon_{p_i} \dfrac{\boldsymbol{B}_i^2}{2} \beta_{\min} + (1 - \Upsilon_{p_i}) p_{o,i} \end{cases}, \text{ if } 1\,R_s \leqslant r \leqslant 2\,R_s. \tag{12}$$

In Equation (12), $\Upsilon_{\rho_i} = 0.5 + 0.5 \tanh\left(\frac{V_{A,i} - V_{A,\max}}{V_{\text{fac}}} \times \pi \right)$ with $V_{A,i} = \frac{|\boldsymbol{B}_i|}{\rho_{o,i}^{0.5}}$, $V_{A,\max} = 2\frac{|\boldsymbol{B}_{\max}|}{\rho_s^{0.5}}$, and $V_{\text{fac}} = \frac{V_{A,\max}}{1000}$. $|\boldsymbol{B}_{\max}|$ represents the maximum magnetic field strength in the entire computational domain. Moreover, $\Upsilon_{p_i} = 0.5 + 0.5 \tanh\left(\frac{\beta_{\min} - \frac{p_i}{0.5\boldsymbol{B}_i^2 + \epsilon}}{\beta_{\text{fac}}} \times \pi \right)$ with $\beta_{\text{fac}} = 10^{-7}$, $\beta_{\min} = 10^{-4}$, and $\epsilon = 10^{-12}$ are adopted in this paper. Additionally, we constrain the plasma velocity in the range $1\,R_s \leqslant r \leqslant 1.1\,R_s$ not to exceed the speed of sound $C_{s,i} = \left(\frac{\gamma p_i}{\rho_i} \right)^{0.5}$, as described in Equation (13):

$$\boldsymbol{v}_i = \boldsymbol{v}_{o,i} \times \min\left(\frac{C_{s,i}}{|\boldsymbol{v}_{o,i}|} \times \left(0.3 + \tanh\left(\frac{r - R_s}{R_s} \times 8.68 \right) \right), 1.0 \right), \quad \text{if } 1\,R_s \leqslant r \leqslant 1.1\,R_s. \tag{13}$$

Here, ρ, p, and $\boldsymbol{v}$ with the subscript "$_o$" denote the density, thermal pressure, and velocity updated during the pseudotime iterations without adjustment.

During the time-evolving coronal simulation, the time step is gradually increased from an explicit time step to τ_{flow}, a reference time that is the same as defined by X. S. Feng et al. (2021) and H. P. Wang et al. (2022a). Additionally, we noticed that during the long-term time-evolving simulations, a dramatic increase in the magnetograms, where the maximum magnetic field strength increases by more than 1.5 times, may occur between two adjacent magnetograms, potentially causing the code to crash. In this paper, this phenomenon occurred in the magnetograms at the 882nd and 888th hours of the approximately 1300 hr time-evolving simulation. Assuming such cases occur at a moment between t_{m-1} and t_m, where the subscripts "$_{m-1}$" and "$_m$" correspond to the $(m-1)$th and mth magnetograms, we opt to employ a second-order Runge–Kutta method, with the intermediate states $\boldsymbol{U}^{(1)}$ and $\boldsymbol{U}^{(2)}$ computed using the backward Euler method (X. S. Feng et al. 2021; H. P. Wang et al. 2022a, 2022b), to solve Equation (6) over the time interval from t_{m-2} to t_{m+3}:

$$\begin{aligned} \boldsymbol{U}_i^{(1)} &= \boldsymbol{U}_i^n - \Delta t \boldsymbol{R}_i^{(1)}, \\ \boldsymbol{U}_i^{(2)} &= \boldsymbol{U}_i^{(1)} - \Delta t \boldsymbol{R}_i^{(2)}, \\ \boldsymbol{U}_i^{n+1} &= \tfrac{1}{2}(\boldsymbol{U}_i^n + \boldsymbol{U}_i^{(2)}). \end{aligned} \tag{14}$$

During this time interval, the inner-boundary magnetic fields between t_{m-2} and t_{m+1} are linearly interpolated from the magnetograms at t_{m-2} and t_{m+1}.

2.4. Implementation of Inner Boundary Conditions

In this paper, we first perform a quasi-steady-state coronal simulation constrained by a time-invariant magnetogram (H. P. Wang et al. 2022a), and then evolve the magnetograms to drive the subsequent time-evolving coronal simulation during CRs 2110 and 2111. Around this period, the time interval between two adjacent GONG-ADAPT magnetograms is 6 hr. The original GONG-ADAPT magnetograms adopted in this paper are positioned in the corotating Carrington heliographic coordinate system. Therefore, we first rotated these magnetograms to the heliocentric inertial coordinate system to match the inertial coordinate system. Subsequently, cubic Hermite interpolation is applied to these input magnetograms to derive the required inner-boundary magnetic fields for each time step during the time-evolving coronal simulations (H. P. Wang et al. 2025b).

As done by H. P. Wang et al. (2025a), the inner boundary conditions are specified at the inner boundary face, which coincides with the solar surface. Four Gaussian points are used on each inner boundary face. The inner boundary conditions at these Gaussian points, together with the solutions in the boundary cell and its 17 neighboring cells that share at least a vertex with it, are utilized to construct the reconstruction formulation of primitive variables in the inner boundary cells (X. S. Feng et al. 2021; H. P. Wang et al. 2025a). For convenience of description, we take the ith boundary cell, denoted as cell BD,i, which is a hexahedral cell consisting of one curved boundary surface and five planar faces (X. S. Feng et al. 2021; H. P. Wang et al. 2022a), as an example. The reconstruction formulations of primitive variables within cell BD,i are presented as follows:

$$X_{\text{BD},i}(\boldsymbol{x}) = X|_{\text{BD},i} + \psi_{\text{BD},i}(\nabla X)|_{\text{BD},i} \cdot (\boldsymbol{x} - \boldsymbol{x}_{\text{BD},i}), \quad X \in \{\rho, u, v, w, \boldsymbol{B}_1, \boldsymbol{B}_{00}, \boldsymbol{B}_0, p, T\}. \tag{15}$$

The subscript "BD,i" refers to the variable corresponding to the ith boundary cell BD,i.

As the inner boundary magnetic field evolves, a tangential component of the electric field, $\boldsymbol{E}_{\text{BD},t} = (E_{\text{BD},\theta}, E_{\text{BD},\phi})$, arises at the inner boundary. Consequently, the corresponding

tangential velocity component, $\boldsymbol{v}_{\mathrm{BD},t} = (v_{\mathrm{BD},\theta}, v_{\mathrm{BD},\phi})$ is given by

$$v_{\mathrm{BD},\theta} = \frac{E_{\mathrm{BD},\phi}}{B_{\mathrm{BD},r}},\ v_{\mathrm{BD},\phi} = -\frac{E_{\mathrm{BD},\theta}}{B_{\mathrm{BD},r}}, \tag{16}$$

ensuring that the flux evolution match the changes of the observed radial magnetic field (L. P. Yang et al. 2012; X. S. Feng et al. 2023). Here, the subscripts "$_\theta$" and "$_\phi$" denote the respective velocity and magnetic field components along the θ and ϕ directions. Additionally, following R. Lionello et al. (2023), we apply the following adjustment to Equation (16) to regularize the flow near the boundary polarity inversion line, where $B_{\mathrm{BD},r} = 0$:

$$\boldsymbol{v}_{\mathrm{BC},t} = \frac{(\boldsymbol{E}_{\mathrm{BC}} \times \boldsymbol{B}_{\mathrm{BC}})_t}{\boldsymbol{B}_{\mathrm{BC}}^2 + D\,|\boldsymbol{E}_{\mathrm{BC}}| \cdot |\boldsymbol{B}_{\mathrm{BC}}|/C_s}. \tag{17}$$

This means that the magnitude of the tangential velocity will converge to C_s/D, where $D = 3$ is adopted in this paper, and C_s is the local sound speed calculated from the solution in the cell immediately adjacent to the inner boundary cell in the radial direction.

During the simulations, the boundary conditions for thermal pressure p_{BD}, plasma density ρ_{BD}, temperature T_{BD}, and radial velocity $v_{\mathrm{BD},r}$ are classified into two cases based on the radial velocity v_r in the cell immediately adjacent to the inner boundary cell in the radial direction (C. P. T. Groth et al. 2000; X. S. Feng et al. 2021; H. P. Wang et al. 2022a, 2022b, 2025a).

(i) $v_r \geqslant 0$: The thermal pressure and plasma density at the inner boundary face are set as $p_{\mathrm{BD}} = 1/\gamma$ and $\rho_{\mathrm{BD}} = 1$ in code units. Following M. Brchnelova et al. (2023) and H. P. Wang et al. (2025b), the inner boundary density ρ_{BD} is further adjusted based on the local Alfvén speed, as in Equation (12), to enhance the PP property of the coronal model. Additionally, the inner boundary temperature is calculated as $T_{\mathrm{BD}} = \frac{\gamma p_{\mathrm{BD}}}{\rho_{\mathrm{BD}}}$, and the radial velocity component is constrained as $\frac{\partial v_{\mathrm{BD},r}}{\partial r} = 0$.

(ii) $v_r \leqslant 0$: $\frac{\partial \rho_{\mathrm{BD}}}{\partial r} = 0$, $\frac{\partial p_{\mathrm{BD}}}{\partial r} = 0$, $\frac{\partial T_{\mathrm{BD}}}{\partial r} = 0$, and $v_{\mathrm{BD},r} = 0$ are applied.

Additionally, the variables at the centroid of inner boundary cells are required to calculate Equation (15). This paper generates the magnetic field from the potential field solver with a 15-order spherical harmonic expansion. The tangential velocity is computed as an average of the values at four Gaussian points and at the centroid of the neighboring cell immediately adjacent to the inner boundary cell in the radial direction. The radial velocity, thermal pressure, plasma density, and temperature are derived using Parker's one-dimensional hydrodynamic isothermal solar wind solution (E. N. Parker 1963). Additionally, the thermal pressure and plasma density are adjusted using Equation (12).

2.5. Derivation of the Extended Decomposed MHD Equations

Considering that $(\boldsymbol{B} + \epsilon\boldsymbol{B})^2 - \boldsymbol{B}^2 \equiv 2\,\epsilon\boldsymbol{B}^2 + \epsilon^2\boldsymbol{B}^2$ with $\epsilon\boldsymbol{B}$ denoting the discretization error in the magnetic field $\boldsymbol{B}$, the magnetic pressure discretization error can be comparable to the thermal pressure in low-β regions, and nonphysical negative thermal pressures are prone to appear when deriving the thermal pressure from energy density. To avoid such undesirable situations, traditional decomposed MHD equations are commonly used, where the magnetic field $\boldsymbol{B}$ is divided into a time-independent potential field and a time-dependent field $\boldsymbol{B}_1$, with $\boldsymbol{B}_1$ being used in the derivation of the thermal pressure. However, discretization errors in $\boldsymbol{B}_1$ are still likely to result in nonphysical negative thermal pressure as $|\boldsymbol{B}_1|$ increases in the time-evolving simulations, potentially causing the code to break down. Therefore, we propose the extended magnetic field decomposition strategy, in which the magnetic field $\boldsymbol{B}$ is divided into a time-independent potential field $\boldsymbol{B}_{00}$, a temporally piecewise-constant field $\boldsymbol{B}_{01}$, and a time-dependent field $\boldsymbol{B}_1$. In the following, we describe how the extended decomposed MHD equations are derived.

With $\boldsymbol{B}_{00}$ representing a static potential field, and $\boldsymbol{B}_{01}$ being a temporally piecewise-constant field that remains unchanged during the time interval between t^n and t^{n+k}, where the subscripts "^{n}" and "$^{n+k}$" denote the nth and $(n+k)$th time levels in a simulation, the following conditions are satisfied within the time interval between t^n and t^{n+k}:

$$\begin{cases} \frac{\partial \boldsymbol{B}_{00}}{\partial t} = \boldsymbol{0},\ \nabla \cdot \boldsymbol{B}_{00} = 0,\ \nabla \times \boldsymbol{B}_{00} = 0,\ t \in [t^n, t^{n+k}] \\ \frac{\partial \boldsymbol{B}_{01}}{\partial t} = \boldsymbol{0},\ t \in (t^n, t^{n+k}). \end{cases} \tag{18}$$

The original energy equation is described as

$$\frac{\partial E}{\partial t} + \nabla \cdot [(E + p_T)\boldsymbol{v} - \boldsymbol{B}(\boldsymbol{v} \cdot \boldsymbol{B})] = -(\nabla \cdot \boldsymbol{B})\boldsymbol{v} \cdot \boldsymbol{B}, \tag{19}$$

where $E = \frac{p}{\gamma - 1} + \frac{1}{2}\rho\boldsymbol{v}^2 + \frac{1}{2}\boldsymbol{B}^2$ and $p_T = p + \frac{\boldsymbol{B}^2}{2}$. Given that $\boldsymbol{B} = \boldsymbol{B}_{00} + \boldsymbol{B}_{01} + \boldsymbol{B}_1$ and $E_1 = \frac{p}{\gamma - 1} + \frac{1}{2}\rho\,\boldsymbol{v}^2 + \frac{1}{2}\boldsymbol{B}_1^2$, the formulation of E can be described as

$$E = E_1 + \frac{1}{2}\boldsymbol{B}_0^2 + \boldsymbol{B}_0 \cdot \boldsymbol{B}_1, \tag{20}$$

where $\boldsymbol{B}_0 = \boldsymbol{B}_{00} + \boldsymbol{B}_{01}$.

The original induction equation is described as

$$\frac{\partial \boldsymbol{B}}{\partial t} + \nabla \cdot (\boldsymbol{v}\,\boldsymbol{B} - \boldsymbol{B}\,\boldsymbol{v}) = -(\nabla \cdot \boldsymbol{B})\boldsymbol{v}. \tag{21}$$

From Equations (18) and (20) we get

$$\frac{\partial E}{\partial t} = \frac{\partial E_1}{\partial t} + \boldsymbol{B}_0 \cdot \frac{\partial \boldsymbol{B}_0}{\partial t} + \boldsymbol{B}_0 \cdot \frac{\partial \boldsymbol{B}_1}{\partial t} + \boldsymbol{B}_1 \cdot \frac{\partial \boldsymbol{B}_0}{\partial t}, \tag{22}$$

$$\frac{\partial \boldsymbol{B}}{\partial t} = \frac{\partial (\boldsymbol{B}_1 + \boldsymbol{B}_{01})}{\partial t}. \tag{23}$$

From Equations (23) and (21), we get

$$\frac{\partial \boldsymbol{B}_1}{\partial t} = -\nabla \cdot (\boldsymbol{v}\,\boldsymbol{B} - \boldsymbol{B}\,\boldsymbol{v}) - \boldsymbol{v}\,\nabla \cdot \boldsymbol{B} - \frac{\partial \boldsymbol{B}_{01}}{\partial t}. \tag{24}$$

Multiplying both sides of Equation (24) by $\boldsymbol{B}_0$ results in

$$\boldsymbol{B}_0 \cdot \frac{\partial \boldsymbol{B}_1}{\partial t} = -\nabla \cdot (\boldsymbol{v}\,\boldsymbol{B} - \boldsymbol{B}\,\boldsymbol{v}) \cdot \boldsymbol{B}_0 - \boldsymbol{v} \cdot \boldsymbol{B}_0\,\nabla \cdot \boldsymbol{B} - \boldsymbol{B}_0 \cdot \frac{\partial \boldsymbol{B}_{01}}{\partial t}. \tag{25}$$

Considering that

$$[\nabla \cdot (\boldsymbol{v}\,\boldsymbol{B})] \cdot \boldsymbol{B}_0 = (\nabla \cdot \boldsymbol{v})(\boldsymbol{B} \cdot \boldsymbol{B}_0) + (\boldsymbol{v} \cdot \nabla\ \boldsymbol{B}) \cdot \boldsymbol{B}_0$$
$$= \nabla\ \cdot [\boldsymbol{v}\,(\boldsymbol{B} \cdot \boldsymbol{B}_0)] - \boldsymbol{v} \cdot \nabla\ (\boldsymbol{B}_0 \cdot \boldsymbol{B}) + (\boldsymbol{v} \cdot \nabla\ \boldsymbol{B}) \cdot \boldsymbol{B}_0,$$

$$[\nabla \cdot (\boldsymbol{B}\,\boldsymbol{v})] \cdot \boldsymbol{B}_0 = (\nabla \cdot \boldsymbol{B})(\boldsymbol{v} \cdot \boldsymbol{B}_0) + (\boldsymbol{B} \cdot \nabla\ \boldsymbol{v}) \cdot \boldsymbol{B}_0$$
$$= \nabla\ \cdot [\boldsymbol{B}\,(\boldsymbol{v} \cdot \boldsymbol{B}_0)] - \boldsymbol{B} \cdot \nabla\ (\boldsymbol{B}_0 \cdot \boldsymbol{v}) + (\boldsymbol{B} \cdot \nabla\ \boldsymbol{v}) \cdot \boldsymbol{B}_0,$$

Equation (25) is equivalent to

$$\boldsymbol{B}_0 \cdot \frac{\partial \boldsymbol{B}_1}{\partial t} = -\nabla\ \cdot [(\boldsymbol{B} \cdot \boldsymbol{B}_0)\,\boldsymbol{v} - (\boldsymbol{v} \cdot \boldsymbol{B}_0)\,\boldsymbol{B}] - \boldsymbol{v} \cdot \boldsymbol{B}_0\ \nabla\ \cdot \boldsymbol{B} - \boldsymbol{B}_0 \cdot \frac{\partial \boldsymbol{B}_{01}}{\partial t} + \eta, \tag{26}$$

where $\eta = \boldsymbol{v} \cdot \nabla\ (\boldsymbol{B}_0 \cdot \boldsymbol{B})$–$(\boldsymbol{v} \cdot \nabla\ \boldsymbol{B})\ \cdot \boldsymbol{B}_0 - \boldsymbol{B} \cdot \nabla\ (\boldsymbol{B}_0 \cdot \boldsymbol{v}) + (\boldsymbol{B} \cdot \nabla\ \boldsymbol{v}) \cdot \boldsymbol{B}_0$.

From Equations (26) and (22) we obtain

$$\frac{\partial E}{\partial t} = \frac{\partial E_1}{\partial t} - \nabla\ \cdot [(\boldsymbol{B} \cdot \boldsymbol{B}_0)\,\boldsymbol{v} - (\boldsymbol{v} \cdot \boldsymbol{B}_0)\,\boldsymbol{B}] - \boldsymbol{v} \cdot \boldsymbol{B}_0\ \nabla\ \cdot \boldsymbol{B} - \boldsymbol{B}_0 \cdot \frac{\partial \boldsymbol{B}_{01}}{\partial t} + \boldsymbol{B}_0 \cdot \frac{\partial \boldsymbol{B}_0}{\partial t} + \boldsymbol{B}_1 \cdot \frac{\partial \boldsymbol{B}_0}{\partial t} + \eta. \tag{27}$$

From Equations (19) and (20) we obtain

$$\frac{\partial E}{\partial t} = -\nabla\ \cdot \left[\left(E_1 + p + \boldsymbol{B}_0^2 + 2\,\boldsymbol{B}_0 \cdot \boldsymbol{B}_1 + \frac{1}{2}\,\boldsymbol{B}_1^2\right) \times \boldsymbol{v} - (\boldsymbol{v} \cdot \boldsymbol{B})\boldsymbol{B}\right] - \boldsymbol{v} \cdot \boldsymbol{B}\ \nabla\ \cdot \boldsymbol{B}. \tag{28}$$

From Equations (28) and (27) we obtain

$$\frac{\partial E_1}{\partial t} + \nabla\ \cdot \left[\left(E_1 + p + \boldsymbol{B}_0 \cdot \boldsymbol{B}_1 + \frac{1}{2}\,\boldsymbol{B}_1^2\right)\boldsymbol{v} - (\boldsymbol{v} \cdot \boldsymbol{B}_1)\boldsymbol{B}\right] = -\boldsymbol{v} \cdot \boldsymbol{B}_1\ \nabla\ \cdot \boldsymbol{B} + \boldsymbol{B}_0 \cdot \frac{\partial \boldsymbol{B}_{01}}{\partial t} - \left(\boldsymbol{B}_0 \cdot \frac{\partial \boldsymbol{B}_0}{\partial t} + \boldsymbol{B}_1 \cdot \frac{\partial \boldsymbol{B}_0}{\partial t}\right) - \eta. \tag{29}$$

Since $\nabla \cdot \boldsymbol{B}_{00} = 0$ and $\frac{\partial \boldsymbol{B}_0}{\partial t} = \frac{\partial \boldsymbol{B}_{01}}{\partial t}$, we obtain the following decomposed energy equation:

$$\frac{\partial E_1}{\partial t} + \nabla \cdot [(E_1 + p_{T1} + \boldsymbol{B}_1 \cdot \boldsymbol{B}_0)\boldsymbol{v} - \boldsymbol{B}(\boldsymbol{v} \cdot \boldsymbol{B}_1)] = -\boldsymbol{v} \cdot \boldsymbol{B}_1\ \nabla\ \cdot (\boldsymbol{B}_1 + \boldsymbol{B}_{01}) - \boldsymbol{B}_1 \cdot \frac{\partial \boldsymbol{B}_0}{\partial t} - \eta, \tag{30}$$

where $p_{T1} = p + \frac{\boldsymbol{B}_1^2}{2}$. This indicates that the thermal pressure, p, can be determined from E_1. As a result, the accuracy of p is no longer limited by the discretization error of $\boldsymbol{B}$ but rather by that of $\boldsymbol{B}_1$. As long as $\boldsymbol{B}_1$ remains small, the discretization error in $\frac{1}{2}\,\boldsymbol{B}_1^2$ is unlikely to approach the magnitude of the thermal pressure, reducing the risk of nonphysical negative thermal pressure.

The original momentum equation is described as

$$\frac{\partial(\rho \boldsymbol{v})}{\partial t} + \nabla\ \cdot \left[\rho \boldsymbol{v}\,\boldsymbol{v} + \left(p + \frac{\boldsymbol{B}^2}{2}\right)\boldsymbol{I} - \boldsymbol{B}\,\boldsymbol{B}\right] = -(\nabla \cdot \boldsymbol{B})\boldsymbol{B}. \tag{31}$$

Given that $\nabla \times \boldsymbol{B}_{00} \times \boldsymbol{B}_{00} = \nabla \cdot \left(-\frac{1}{2}\boldsymbol{B}_{00}^2\boldsymbol{I} + \boldsymbol{B}_{00}\,\boldsymbol{B}_{00}\right) - (\nabla \cdot \boldsymbol{B}_{00})\,\boldsymbol{B}_{00}$ and $\nabla \cdot \boldsymbol{B}_{00} = 0$, Equation (31) is equivalent to

$$\frac{\partial(\rho\,\boldsymbol{v})}{\partial t} + \nabla \cdot \left[\rho \boldsymbol{v}\,\boldsymbol{v} + \left(p + \frac{\boldsymbol{B}^2}{2} - \frac{\boldsymbol{B}_{00}^2}{2}\right)\boldsymbol{I} - \boldsymbol{B}\,\boldsymbol{B} + \boldsymbol{B}_{00}\,\boldsymbol{B}_{00}\right] = -\nabla\ \cdot (\boldsymbol{B}_1 + \boldsymbol{B}_{01})\boldsymbol{B}. \tag{32}$$

Consequently, we obtain the following extended decomposed MHD equations:

$$\begin{cases} \dfrac{\partial \rho}{\partial t} + \nabla \cdot (\rho\,\boldsymbol{v}) = 0 \\ \dfrac{\partial(\rho\,\boldsymbol{v})}{\partial t} + \nabla \cdot \left[\rho \boldsymbol{v}\,\boldsymbol{v} + \left(p + \dfrac{\boldsymbol{B}^2}{2} - \dfrac{\boldsymbol{B}_{00}^2}{2}\right)\boldsymbol{I} - \boldsymbol{B}\,\boldsymbol{B} + \boldsymbol{B}_{00}\,\boldsymbol{B}_{00}\right] = -\nabla \cdot (\boldsymbol{B}_1 + \boldsymbol{B}_{01})\boldsymbol{B} \\ \dfrac{\partial E_1}{\partial t} + \nabla \cdot [(E_1 + p_{T1} + \boldsymbol{B}_1 \cdot \boldsymbol{B}_0)\boldsymbol{v} - \boldsymbol{B}(\boldsymbol{v} \cdot \boldsymbol{B}_1)] = -\nabla \cdot (\boldsymbol{B}_1 + \boldsymbol{B}_{01})(\boldsymbol{v} \cdot \boldsymbol{B}_1) \\ \quad -\boldsymbol{B}_1 \cdot \dfrac{\partial \boldsymbol{B}_0}{\partial t} - \boldsymbol{v} \cdot \nabla(\boldsymbol{B}_0 \cdot \boldsymbol{B}) + (\boldsymbol{v} \cdot \nabla \boldsymbol{B}) \cdot \boldsymbol{B}_0 + \boldsymbol{B} \cdot \nabla(\boldsymbol{B}_0 \cdot \boldsymbol{v}) - (\boldsymbol{B} \cdot \nabla \boldsymbol{v}) \cdot \boldsymbol{B}_0 \\ \dfrac{\partial \boldsymbol{B}_1}{\partial t} + \nabla \cdot (\boldsymbol{v}\,\boldsymbol{B} - \boldsymbol{B}\,\boldsymbol{v}) = -\nabla \cdot (\boldsymbol{B}_1 + \boldsymbol{B}_{01})\boldsymbol{v} - \dfrac{\partial \boldsymbol{B}_{01}}{\partial t}. \end{cases} \tag{33}$$

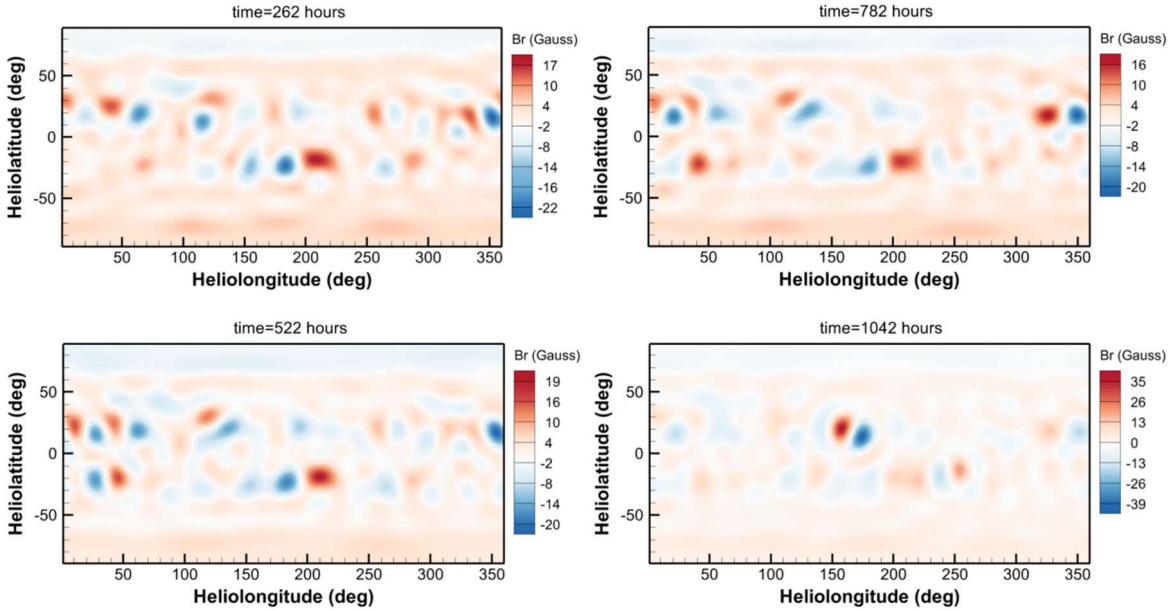

Figure 1. Distribution of the radial magnetic field used as the inner boundary condition at the solar surface, shown in a corotating coordinate system. Its evolution throughout the simulation (from $t = 3$ to 1318) is demonstrated in an animation.
(An animation of this figure is available.)

Moreover, we consider a specific condition in which $\boldsymbol{B}_{01}$ is artificially increased by $\boldsymbol{B}_1$ over an infinitesimally short period denoted by $\lim_{dt\to 0^+} dt$. This adjustment is applied when $\boldsymbol{B}_1$ becomes significantly large at time t^n, such as when $\frac{p}{0.5\,\boldsymbol{B}_1^2}$ drops below a certain threshold. Correspondingly, $\boldsymbol{B}_1$, $\boldsymbol{B}_0$, E_1, and $p_{\rm T1}$ evolve to $\boldsymbol{B}_1^*$, $\boldsymbol{B}_0^*$, E_1^*, and $p_{\rm T1}^*$, respectively, ensuring that the MHD system remains unchanged during the time interval $\lim_{dt\to 0^+} dt$. As a result, Equations (24) and (30) can be described as

$$\lim_{dt\to 0^+}\frac{\boldsymbol{B}_1^*-\boldsymbol{B}_1}{dt} = -\nabla\cdot(\boldsymbol{v}\,\boldsymbol{B}-\boldsymbol{B}\,\boldsymbol{v}) - \boldsymbol{v}\,\nabla\cdot\boldsymbol{B} - \lim_{dt\to 0^+}\frac{\boldsymbol{B}_{01}^*-\boldsymbol{B}_{01}}{dt}, \tag{34}$$

and

$$\lim_{dt\to 0^+}\frac{E_1^*-E_1}{dt} + \nabla\cdot[(E_1^*+p_{T1}^*+\boldsymbol{B}_1^*\cdot\boldsymbol{B}_0^*)\boldsymbol{v}-\boldsymbol{B}(\boldsymbol{v}\cdot\boldsymbol{B}_1^*)] = -\boldsymbol{v}\cdot\boldsymbol{B}_1^*\nabla\cdot(\boldsymbol{B}_1^*+\boldsymbol{B}_{01}^*) - \boldsymbol{B}_1^*\cdot\lim_{dt\to 0^+}\frac{\boldsymbol{B}^*-\boldsymbol{B}}{dt} + \frac{1}{2}\lim_{dt\to 0^+}\frac{|\boldsymbol{B}_1^*|^2-|\boldsymbol{B}_1|^2}{dt} - \eta^*, \tag{35}$$

where $\boldsymbol{B}_{01}^* = \boldsymbol{B}_{01}+\boldsymbol{B}_1$, $\boldsymbol{B}^* = \boldsymbol{B}_0^*+\boldsymbol{B}_1^*$, $p_{\rm T1}^* = p+\frac{1}{2}|\boldsymbol{B}_1^*|^2$, and $\eta^* = \boldsymbol{v}\cdot[\nabla(\boldsymbol{B}_0^*\cdot\boldsymbol{B})] - (\boldsymbol{v}\cdot\nabla\boldsymbol{B})\cdot\boldsymbol{B}_0^* - \boldsymbol{B}\cdot[\nabla(\boldsymbol{B}_0^*\cdot\boldsymbol{v})] + (\boldsymbol{B}\cdot\nabla\boldsymbol{v})\cdot\boldsymbol{B}_0^*$. Consequently, $\boldsymbol{B}_1^*\to\boldsymbol{0}$ can be derived from Equation (34). Keeping in mind that $\boldsymbol{B}_0^* = \boldsymbol{B}_{00}+\boldsymbol{B}_{01}^*$, $\boldsymbol{B}^*\to\boldsymbol{B}$, and $\boldsymbol{B}_0^*+\boldsymbol{B}_1^* = \boldsymbol{B}$, we can derive $E_1^*\to E_1-\frac{1}{2}|\boldsymbol{B}_1|^2$ from Equation (35). At the end of this infinitely short period, $\boldsymbol{B}_{01}$, $\boldsymbol{B}_1$, and E_1 become $\boldsymbol{B}_{01}+\boldsymbol{B}_1$, $\boldsymbol{0}$, and $\frac{p}{\gamma-1}+\frac{1}{2}\rho\mathbf{v}^2$, respectively.

Therefore, when $\frac{p}{0.5\,\boldsymbol{B}_1^2}$ drops below a threshold at time t^n, we update $\boldsymbol{B}_{01}$ to $\boldsymbol{B}_{01}+\boldsymbol{B}_1$, set $\boldsymbol{B}_1 = 0$, and assign $E_1 = \frac{p}{\gamma-1}+\frac{1}{2}\rho\boldsymbol{v}^2$ and $p_{\rm T1} = p$. Subsequently, we solve Equation (33) with $\frac{\partial\boldsymbol{B}_{01}}{\partial t} = 0$ to advance the solutions in time. This process continues until $\frac{p}{0.5\,\boldsymbol{B}_1^2}$ once again drops below the threshold, at which moment we repeat the procedure outlined above.

3. Numerical Results

In this section, the time-evolving SIP-IFVM coronal model, equipped with the extended magnetic field decomposition strategy, is employed to simulate the evolution of coronal structures during CRs 2110 and 2111. This period, spanning from 2011 May 9 to July 3, corresponds to the solar maximum of Solar Cycle 24. Approximately 220 GONG-ADAPT magnetograms,[18] with the first realization of the 12-member ensemble (B. Perri et al. 2023) adopted and updated at a 6 hr cadence, are used to drive these simulations in an inertial coordinate system spanning from the solar surface to 20 R_s. During the time-evolving simulations, the magnetic field near the solar surface sometimes exceeds 40 G, with the plasma β reaching a minimum value of around 10^{-3}. Figure 1 displays the inner boundary magnetic field at various moments. For convenience of comparison, these magnetic field distributions are illustrated in a corotating coordinate system. The figure reveals that the inner-boundary magnetic field varies more significantly at low and middle latitudes, while the regions beyond 70° in both the north and south poles are predominantly occupied by magnetic fields directed inward and outward from the Sun. Additionally, a dipole with a strong magnetic field is observed in the panel at 1042 hr. Video 1 (linked in Figure 1) illustrates the evolution of the ADAPT-GONG maps during this period, suggesting that this dipole may have originated on the Sun's farside and was later updated with nearside data. This leads to the sudden appearance of a

[18] https://gong.nso.edu/adapt/maps/gong/2011/

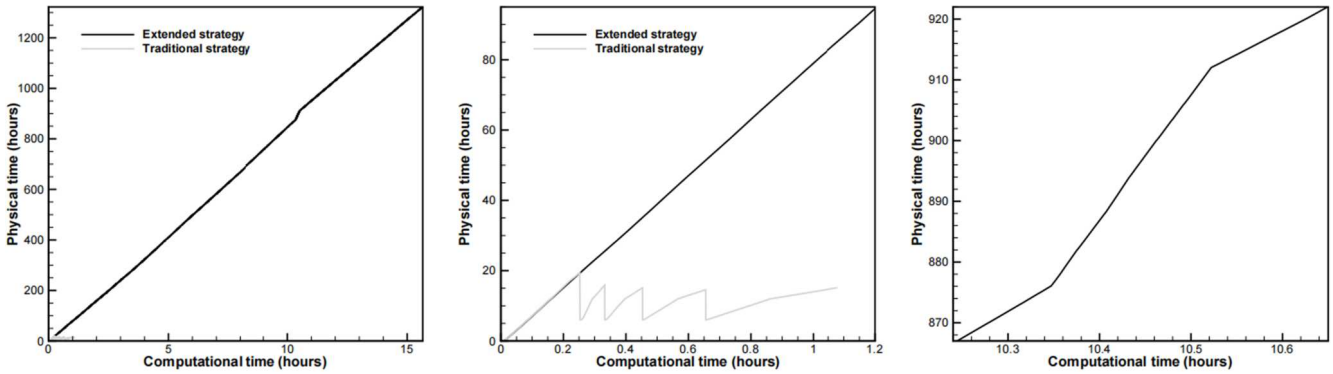

Figure 2. Evolution of physical time vs. computational time in the time-evolving coronal simulation for CRs 2110 and 2111 (left), with close-up views of the profile during the first 1.2 hr (middle) and between 10.24 and 10.65 hr of computational time (right).

dipole with a strong magnetic field on the magnetogram at the 888th hour.

All calculations in this paper are performed on the WICE cluster, part of the Tier-2 supercomputer infrastructure of the Vlaams Supercomputer Centrum (VSC).[19] The simulation consists of 23,040 time steps, with the average time step being approximately 3.4 minutes. Using 192 CPU cores, the wall-clock time for simulating these two solar maximum CR periods is approximately 16 hr. In addition to the simulation using the extended magnetic field decomposition strategy, we also conduct a simulation with the traditional method for comparison. However, the latter crashes after approximately 20 hr of physical time. When the simulation using the traditional method fails at a time step between t_{m-1} and t_m, we restart from t_{m-2} and apply Equation (14) to solve the governing equations, as described in Section 2.3. Simultaneously, we reduce the time-step limit to half of its previous value. If the simulation crashes again within the same interval, we revert to t_{m-2} and further reduce the time-step by half. If the failure persists for four consecutive attempts, the reversion process is discontinued.

Figure 2 illustrates the evolution of physical time versus computational time for both simulations, using the extended magnetic field decomposition strategy (black solid lines) and the traditional method (gray solid lines). The left panel demonstrates that the evolution of coronal structures over 1322 hr of physical time is completed within just 16 hr of computational time, showcasing that our model with the extended magnetic field decomposition strategy operates over 80 times faster than real-time coronal evolution using only 192 CPU cores. The right panel, a close-up view of the profile between 876 and 912 hr of physical time, is around the event of a dramatic increase in the magnetograms described in Section 2.3 and is completed within 0.18 computational hours, demonstrating an efficiency approximately 1.5 times greater than during other periods. Although the strategy outlined in Equation (14) may overlook some high-frequency phenomena during this interval and reduce temporal accuracy, it effectively prevents simulation crashes during periods of dramatic increases in inner-boundary magnetic field strength. Furthermore, the middle panel shows that the simulation using the traditional method crashed after around 20 hr of physical time, even with a small time step. This highlights the effectiveness of the extended magnetic field decomposition strategy in handling time-evolving low-β issues.

3.1. Distributions of the Open and Closed Magnetic Field Regions

Coronal holes (CHs) are dark regions observed in extreme ultraviolet (EUV) and soft X-ray channels, typically associated with low plasma density and magnetic field lines that are open to interplanetary space. CH distributions vary across different phases of solar activity and are among the most prominent features of the solar corona (G. J. D. Petrie et al. 2011; X. S. Feng et al. 2015, 2017, 2019). Generally, three types of CHs can be identified in EUV and soft X-ray images of the solar corona. Polar CHs are located at the solar poles and often extend to lower latitudes, occasionally crossing the solar equator. Isolated CHs, commonly observed near solar maxima, are detached from polar CHs and scattered across low and mid-latitudes. Transient CHs are associated with solar eruptive events, such as CMEs, solar flares, and eruptive prominences.

In Figure 3, we derive the simulated open- and closed-field regions by tracing the magnetic field lines from 2.5 R_s to the solar surface (middle and bottom panels) and compare them with the synoptic maps of the observations (top panel) from the 193 Å channel of the Atmospheric Imaging Assembly (AIA) instrument (J. R. Lemen et al. 2012) on board the Solar Dynamics Observatory (SDO) satellite (W. D. Pesnell et al. 2012).[20] These images are illustrated in a corotating coordinate system with these synoptic images generated by concatenating a series of meridional strips extracted from full-disk images over the duration of a complete CR (A. Hamada et al. 2018). They reveal that the simulations adequately reproduce the observed southern polar CH from latitude 70° poleward. The leading CHs around 220° and 280° in longitude, extending from the southern pole to near the solar equator, as well as the isolated CH centered at ($\theta_{\rm lat}$, $\phi_{\rm long}$) = (40°N, 60°) and detached from the northern polar CH, are also well captured. Here, "$\theta_{\rm lat}$" represents the heliographic latitude, and "$\phi_{\rm long}$" denotes the Carrington longitude. Additionally, the decreasing trend of scattered isolated CHs in the low-latitude domain from CR 2110 to 2111 is also captured in the simulation results. Notably, the isolated CH centered around ($\theta_{\rm lat}$, $\phi_{\rm long}$) = (0°, 150°) rapidly transformed from an upside-down hook shape at 782 hr to a whirlwind-like structure above the solar equator at 1042 hr. Together with Figure 1, this rapid change can be attributed primarily to the emergence of a dipole centered at ($\theta_{\rm lat}$, $\phi_{\rm long}$) = (10°N, 160°).

[19] https://www.vscentrum.be/

[20] https://sdo.gsfc.nasa.gov/data/synoptic/

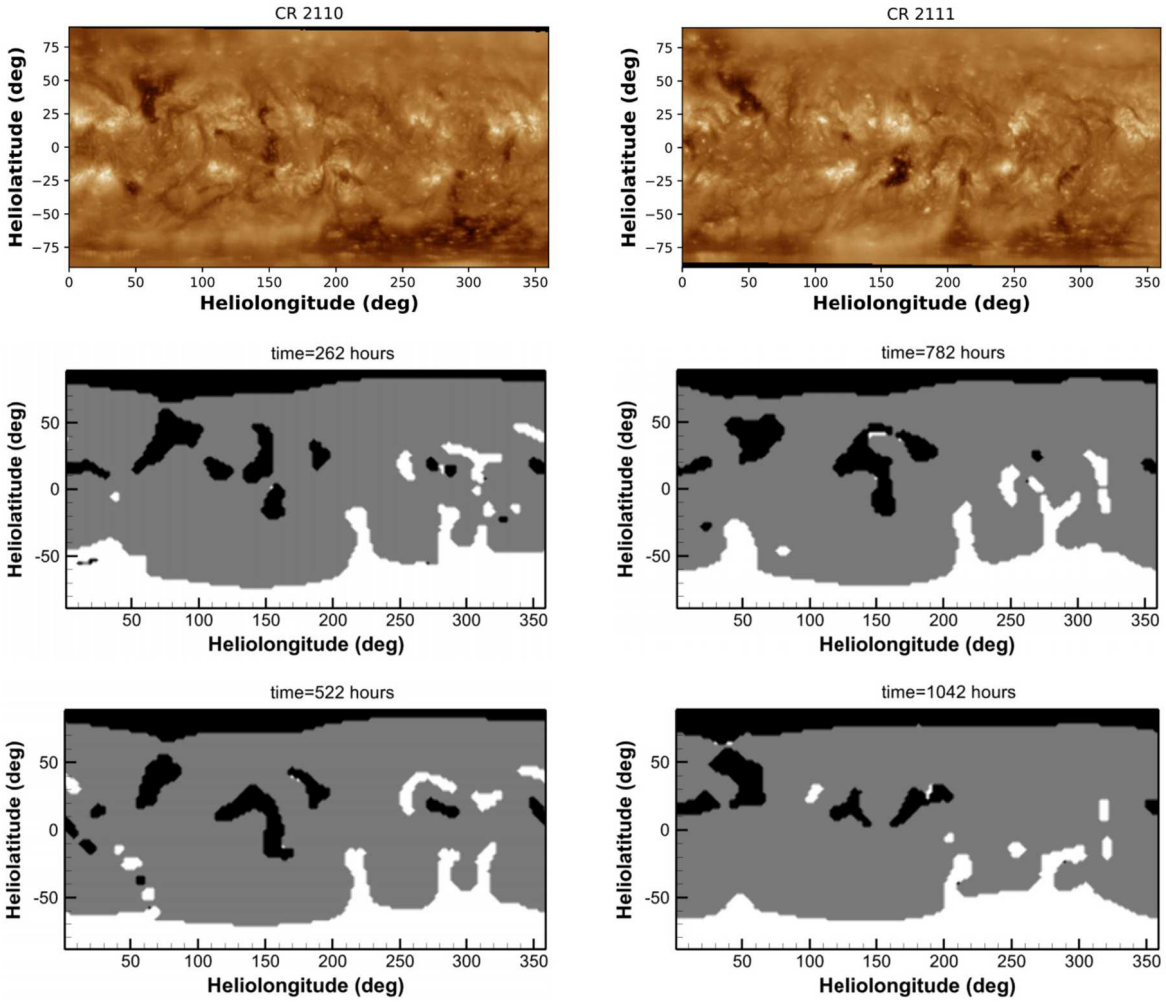

Figure 3. Synoptic maps of the EUV observations from the 193 Å channel of AIA on board SDO (top) for CRs 2110 (left) and 2111 (right), alongside the distributions of open- and closed-field regions modeled by the time-evolving SIP-IFVM coronal model (middle and bottom), all shown in a corotating coordinate system. In the middle and bottom panels, the white and black patches represent open-field regions with magnetic field lines pointing outward and inward relative to the Sun, respectively, while the gray patches indicate closed-field regions.

In Figure 4, we present the synthesized 171 Å EUV images in a corotating coordinate system. The synthesized EUV images are derived by integrating the emission along the radial direction from 1.02 R_s to 1.5 R_s. The emission at each point $\boldsymbol{x}$ of our computational domain is calculated via

$$I_\lambda(\boldsymbol{x}) = G_\lambda(T, n_e) n_e^2(\boldsymbol{x}),$$

where the wavelength $\lambda = 171$ Å and G_λ is the temperature-dependent response function for the 171 Å wave band, which is obtained from the CHIANTI atomic database (K. P. Dere et al. 1997, 2023). The 171 Å EUV images primarily show the solar corona at temperatures of approximately 0.8–1.0 MK. Since the lifetime of coronal loops typically ranges from minutes to hours (F. Reale 2014), and cannot be resolved by the six-hourly updated synoptic magnetograms, the simulation results cannot accurately reproduce the bright structures observed in the AIA 171 Å EUV images. Therefore, we do not compare our results with the AIA 171 Å EUV observations. Alternatively, we compare them with the distributions of the open magnetic field regions in Figure 3.

It can be seen that dark regions occupy the open-field polar region in Figure 3 in the 171 Å EUV images. At 262 hr, the dark regions centered at ($\theta_{\rm lat}$, $\phi_{\rm long}$) = (15°N, 50°), ($\theta_{\rm lat}$, $\phi_{\rm long}$) = (15°S, 150°), (20°S, 215°) and ($\theta_{\rm lat}$, $\phi_{\rm long}$) = (15°S, 280°) align with open-field regions, whereas the dark region centered at ($\theta_{\rm lat}$, $\phi_{\rm long}$) = (40°N, 40°) corresponds to a closed-field region. At 522 hr, the dark regions centered at ($\theta_{\rm lat}$, $\phi_{\rm long}$) = (20°S, 45°), ($\theta_{\rm lat}$, $\phi_{\rm long}$) = (20°S, 150°), (25°N, 250°) and ($\theta_{\rm lat}$, $\phi_{\rm long}$) = (10°N, 280°) align with open-field regions, whereas the dark region centered at ($\theta_{\rm lat}$, $\phi_{\rm long}$) = (45°S, 170°) corresponds to a closed-field region. At 782 hr, the dark regions centered at ($\theta_{\rm lat}$, $\phi_{\rm long}$) = (20°S, 210°) and ($\theta_{\rm lat}$, $\phi_{\rm long}$) = (20°S, 285°) align with open-field regions, while the dark region centered at ($\theta_{\rm lat}$, $\phi_{\rm long}$) = (25°N, 100°) corresponds to a closed-field region. At 1042 hr, the dark regions centered at ($\theta_{\rm lat}$, $\phi_{\rm long}$) = (20°S, 215°), ($\theta_{\rm lat}$, $\phi_{\rm long}$) = (10°S, 255°) and ($\theta_{\rm lat}$, $\phi_{\rm long}$) = (15°N, 320°) align with open-field regions, whereas the dark region centered at ($\theta_{\rm lat}$, $\phi_{\rm long}$) = (20°S, 60°) corresponds to a closed-field region. Additionally, the extremely bright region centered at ($\theta_{\rm lat}$, $\phi_{\rm long}$) = (15°S, 170°) may be attributed to the transition of the open-field region in this area around 782 hr to a closed-field configuration at 1042 hr. This demonstrates that most of the dark regions in these synthesized 171 Å EUV images correspond to open-field regions, while the bright regions are associated with closed-field regions. The discrepancies may be

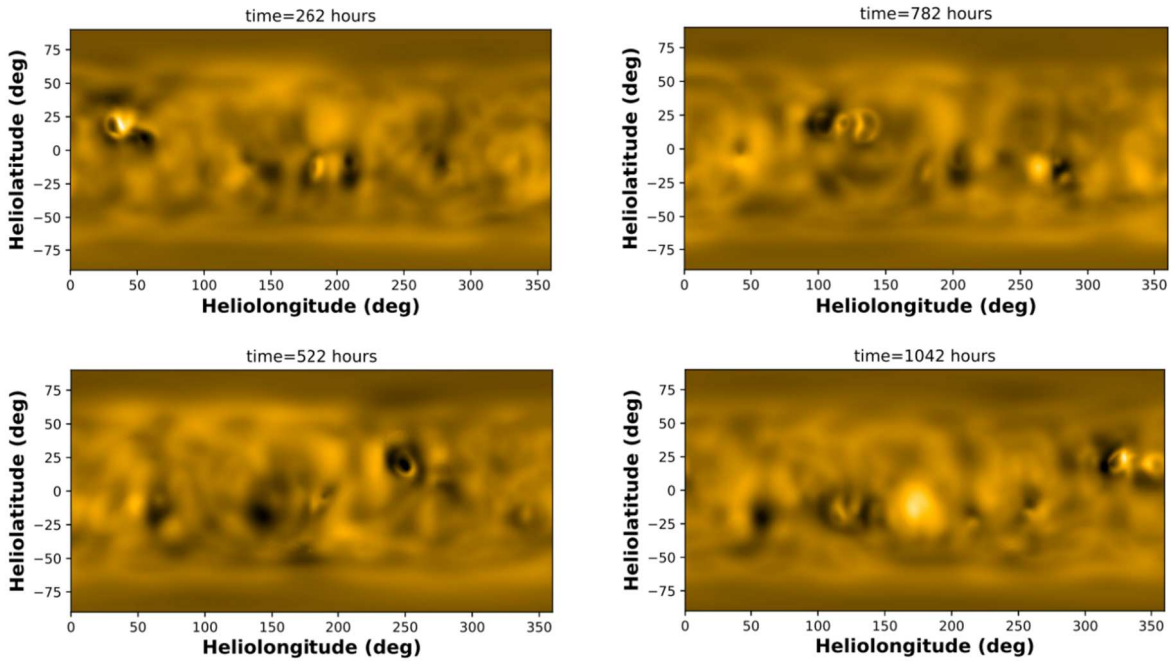

Figure 4. Synoptic maps of the EUV images derived from the time-evolving simulation results at four different moments.

attributed to the relatively low resolution of the computational mesh, the lack of a self-consistent heating mechanism, and the fact that dark regions in EUV maps do not necessarily correspond to open-field regions (M. A. Reiss et al. 2024).

3.2. Time-evolving Coronal Structures

White-light polarized brightness (pB) images can reveal various large-scale coronal structures. In these pB images, bright regions correspond to high-density coronal structures, such as bipolar and pseudostreamers. In contrast, dark regions indicate low-density structures, such as coronal holes (X. S. Feng et al. 2015, 2017, 2019; X. S. Feng 2020). Bipolar streamers separate CHs with opposite magnetic polarities, while pseudostreamers separate CHs of the same polarity. Additionally, bipolar streamers extend outward several solar radii from the Sun, forming a cusplike structure as they are drawn into a current sheet above the helmet streamer (Y. M. N. R. Wang et al. 2007; X. S. Feng et al. 2017, 2019).

In Figure 5, we compare white-light pB images from the innermost coronagraph of the Sun Earth Connection Coronal and Heliospheric Investigation (SECCHI) instrument suite (top) on board the Solar Terrestrial Relations Observatory Ahead (STEREO-A) spacecraft[21] (R. A. Howard et al. 2008) with those synthesized from the simulation results ranging from 2.5 R_s to 15 R_s (middle). The 2D distributions of some selected simulated magnetic field lines on the meridional plane in the STEREO-A view, ranging from 1 R_s to 6 R_s, are also illustrated (bottom). This comparison indicates that the simulated magnetic field lines and bright structures are generally consistent with the observed bipolar and pseudostreamers. However, some discrepancies exist in the width and position of these bright structures. The mismatch may come from the imperfect measurements of photospheric magnetic fields and the possible presence of solar disturbances during the two CRs that are not considered in the MHD modeling.

At 442 hr into the time-evolving coronal simulation, corresponding to 2011 May 28, both the simulation and observation exhibit two bright structures centered around 44°S and 46°N at the east and west limbs, respectively. The magnetic field lines indicate that bipolar streamers form these bright structures. However, in the simulation, the observed bright structures centered around 10°N and 20°S at the east and west limbs are shifted northward by approximately 40° and 20°, respectively. At 602 hr, corresponding to 2011 June 3, the three bright structures centered around 22°S at the east limb and 57°N and 7°N at the west limb are well reproduced in the simulation, formed by bipolar streamers. However, the pseudostreamers located around 34°S and 61°N at the west and east limbs appear 10° and 20° farther north than in the observations. At 1102 hr, corresponding to 2011 June 24, the simulated bipolar streamer around 12°S at the west limb successfully captured the observed bright structure, while the simulated bipolar streamer around 22° S at the east limb is shifted 20° northward compared to observations. Additionally, the pseudostreamers around 48°N at both limbs align well with the observed bright structures. At 1262 hr, corresponding to 2011 July 1, the simulated bipolar streamer around 20°S at the east limb and 6°N at the west limb effectively reproduced the observed structures. The pseudostreamers around 45°N and 59°N at the west and east limbs also closely match the observations. However, the observed bright structure around 18°S is not present in the simulation results despite the existence of a pseudostreamer in the magnetic field structure.

Additionally, we compare the pB observations at 3 R_s with the modeled results in Figure 6. The top panels illustrate synoptic maps of the east-limb observations from the Large Angle and Spectrometric Coronagraph C2 (LASCO-C2) (G. E. Brueckner et al. 1995) on board the Solar and Heliospheric Observatory (SOHO)[22] for CRs 2110 (left) and 2111 (right), with the bright structures representing distributions of the high-density coronal structures. The middle and bottom panels display the 2D timing diagrams of simulated plasma number density

[21] https://stereo-ssc.nascom.nasa.gov/browse/

[22] https://sdo.gsfc.nasa.gov/data/synoptic/

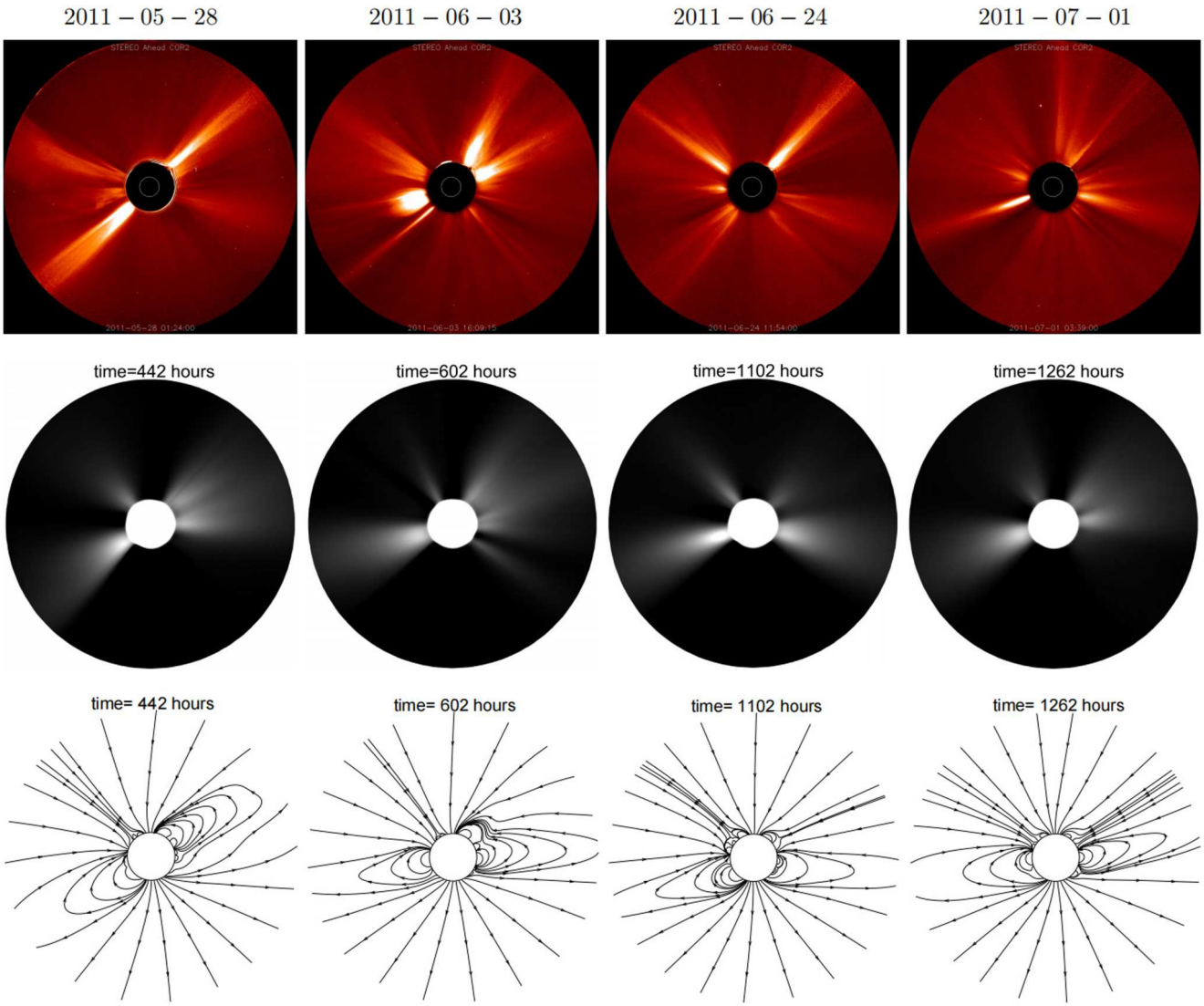

Figure 5. White-light pB images observed by COR2/STEREO-A (top), ranging from 2.5 R_s to 15 R_s, alongside corresponding pB images synthesized from simulation results ranging from 2.5 R_s to 15 R_s (middle) and 2D distributions of some selected simulated magnetic field lines from 1 R_s to 6 R_s (bottom). These images are shown on the meridional plane in the STEREO-A view.

($10^5\,\mathrm{cm}^{-3}$) and radial velocity V_r ($\mathrm{km\,s}^{-1}$). These 2D timing diagrams are synthesized from a series of time-evolving simulation results with a cadence of one result per 20 hr. The radial basic function interpolation method (H. P. Wang et al. 2022a) is applied to interpolate the variables to the east-limb longitude of the Sun in the Earth view. The orange solid lines overlaid on these counter denote the magnetic neutral lines (MNLs) modeled by the time-evolving coronal model.

The comparison in Figure 6 demonstrates that the bright structures in the simulated plasma density are generally consistent with those in the pB observations. The simulated high-density, low-speed flows are primarily distributed around the MNLs. Additionally, it can be noted that the northernmost bright structures in the simulation for CR 2110 extend approximately 20° farther north during the first 320 hr. Meanwhile, for CR 2111, the bright structures during the first 270 hr of the simulation changed from a trapezoidal cavity to irregular solid triangles in the observations. These mismatches may be attributed to the fact that the magnetic field at different longitudes in each synoptic magnetograph is observed at different times, as well as the imperfect measurements of the photospheric magnetic fields in the polar regions.

During the time-evolving coronal simulation, two virtual satellites are placed at 3 R_s and 20 R_s, maintaining the same latitude as Earth and lagging 60° behind in longitude. In Figure 7, we present the timing diagrams of radial velocity V_r ($\mathrm{km\,s}^{-1}$, left), proton number density ($10^5\,\mathrm{cm}^{-3}$ at 3 R_s and $10^3\,\mathrm{cm}^{-3}$ at 20 R_s, middle), and decadic logarithms of plasma β (top right) and radial magnetic field polarities (bottom right), as monitored by the virtual satellites positioned at 3 R_s (top) and 20 R_s (bottom).

The top panels of Figure 7 indicate that the plasma β at 3 R_s around the solar equator usually varies between 0.3 and 100 during the time-evolving simulation, which is consistent with the values derived by G. A. Gary (2001). It is also observed that a peak/trough in the plasma density profile generally corresponds to a trough/peak in the velocity profile. However, the peaks in plasma density around 600 and 675 hr are narrower than the corresponding troughs in the velocity profile, while the trough in plasma density around 850 hr is

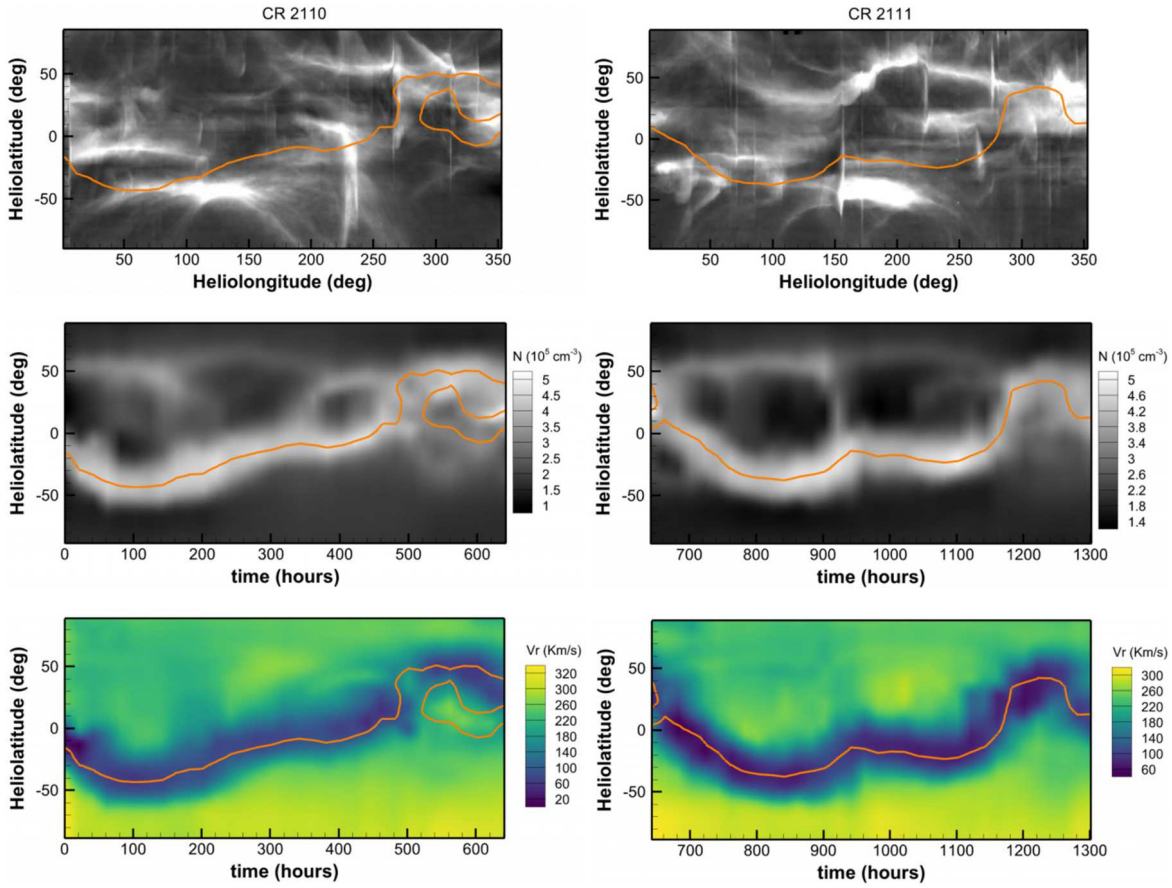

Figure 6. Synoptic maps of east-limb white-light pB images at 3 R_s observed by the LASCO-C2 instrument on board the SOHO satellite (top) for CRs 2110 (left) and 2111 (right), alongside the timing diagrams of simulated plasma number density (10^5 cm^{-3}) and radial velocity V_r (km s^{-1} at 3 R_s at the east-limb longitude of the Sun in the Earth view.

broader than the corresponding velocity peak. These mismatches reveal the complexity of dynamic mechanisms in the subsonic/sub-Alfvénic coronal region, highlighting the requirement for careful consideration of the transformation between kinetic and magnetic energy in simulations of such regions.

At 20 R_s, the velocity peaks and troughs align more closely with plasma density troughs and peaks, indicating that the dynamics in this supersonic/super-Alfvénic region are significantly simpler than those in the subsonic/sub-Alfvénic coronal region. Additionally, we noticed that the two velocity troughs appearing around 740.5 and 166.5 hr at 3 R_s shifted to 748.2 and 175.0 hr at 20 R_s, respectively. This indicates that the two troughs propagate from 3 R_s to 20 R_s with an average velocity of approximately 350 km s^{-1}. By performing a ballistic propagation, we map the solar wind velocity and radial magnetic field polarities observed by the Wind satellite[23] (J. H. King & N. E. Papitashvili 2005) at 1 au to 20 R_s (top, gray solid lines). Considering that some velocity peaks observed at 1 au appear roughly 100 hr earlier when mapped to 20 R_s, we positioned the virtual satellite 60° behind Earth to compare with in situ observations at 1 au near Earth.

The bottom panels of Figure 7 show that the simulation captures the observed velocity peaks around 73 hr and 750 hr. The simulated velocity peak, approximately 580 km s^{-1}, occurs at 280 hr in the simulation, while it appears at 410 hr in the observations. Additionally, the velocity exceeding 580 km s^{-1}, which persists between 370 and 410 hr in the observations, is missing in the simulation. The observed velocity peak around 1000 hr appears about 70 hr earlier than in the simulation. Additionally, the simulation approximately captures the observed velocity troughs around 180 hr and 880 hr. The two observed velocity troughs, centered at 500 and 650 hr, combine into one wide trough in the simulation, while the observed trough centered at 1100 hr occurs about 150 hr earlier than in the simulation. As for the radial magnetic polarities, the simulation captures 83.4% of the observations. These discrepancies in velocity and radial magnetic polarities may be attributed to the limitations of the empirical heating function used to approximate coronal heating and solar wind acceleration, as well as the constraints of synoptic magnetograms, where the magnetic field at different longitudes is observed at different times. Since this period occurs during solar maximum, the frequent eruptions, such as coronal mass ejections, which are not included in this model, may also contribute to the discrepancies between the simulation results and observations.

In Figure 8, we further present the 2D timing diagrams of simulated plasma number density (10^3 cm^{-3}, top), radial velocity V_r (km s^{-1}, middle), and temperature (10^5 K, bottom) to show whether the code produces the latitudinal structure of the solar wind, which is basically the latitude distribution of the fast and slow solar wind. These diagrams are synthesized from a series of time-evolving simulation results at the same

[23] https://cdaweb.gsfc.nasa.gov/index.html

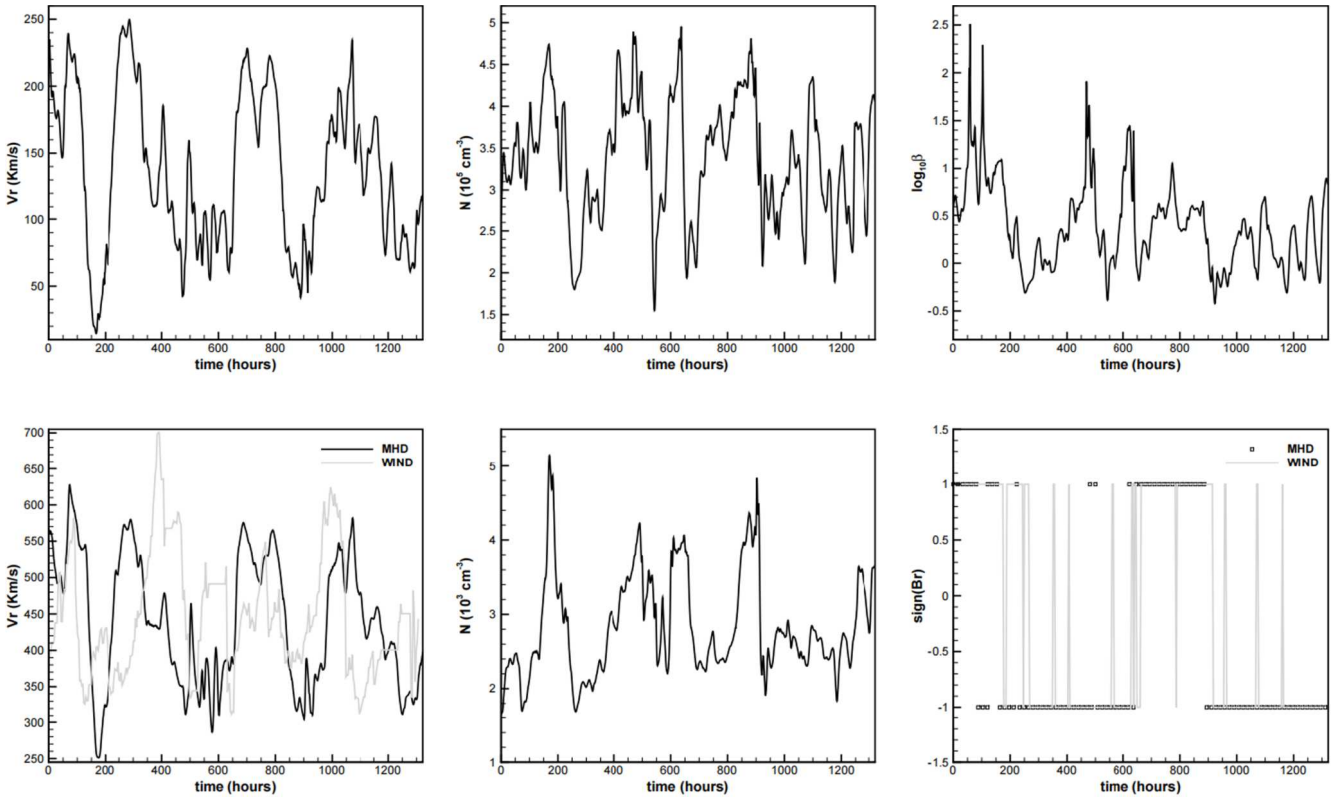

Figure 7. Timing diagram of radial velocity V_r (km s^{-1}, left), proton number density (10^5 cm^{-3} at 3 R_s and 10^3 cm^{-3} at 20 R_s, middle), and decadic logarithms of plasma β (top right) and radial magnetic field polarities (bottom right) with "−1" denoting the field pointing to the Sun and "1" for the field directed away from the Sun, as observed by a virtual satellite located at 3 R_s (top) and 20 R_s (bottom), positioned at 60° behind Earth in longitude and at the same latitude. The black solid lines and black square symbols represent the simulated variables, while the gray solid lines indicate the variables derived from Wind satellite observations, which have been mapped from 1 au to 20 R_s following the ballistic propagation.

longitude as the virtual satellite, with a cadence of one result every 20 hr. The solid orange lines overlaid on the contours represent the MNLs. They show that the MNLs, spanning between 30°S and 45°S, are flatter than those in Figure 6. The low-speed solar wind ($V_r < 400\,\mathrm{km\,s^{-1}}$), associated with high plasma density, is primarily concentrated around the MNLs. Meanwhile, the fast solar wind ($V_r > 550\,\mathrm{km\,s^{-1}}$), accompanied by low plasma density, dominates the polar regions south of 50°S and north of 80°N. The simulated plasma temperature distributions are positively correlated with radial solar wind speeds (H. A. Elliott et al. 2012; R. F. Pinto & A. P. Rouillard 2017; C. X. Li et al. 2018), with the fast solar wind exhibiting temperatures ranging from 1 to 1.5 MK, while the slow wind corresponds to temperatures between 0.3 and 0.7 MK. This demonstrates that the simulated temperature range matches observations.

4. Concluding Remarks

In this work, we extended our recently developed SIP-IFVM model (H. P. Wang et al. 2025a), an implicit MHD coronal model constrained by a time-invariant magnetogram, into a time-evolving coronal model. We adjusted the adiabatic index γ from 1.05 to 5/3 to better represent the adiabatic process in coronal simulations. Furthermore, we designed a magnetic field decomposition strategy for time-evolving coronal simulations and applied it to the time-evolving SIP-IFVM coronal model. Our approach introduces a temporally piecewise-constant variable to accommodate part of the nonpotential field, ensuring that $\boldsymbol{B}_1$ remains consistently small throughout the simulations. As a result, the occurrence of nonphysical negative thermal pressure when deriving thermal pressure from energy density in low-β regions was effectively mitigated in time-evolving coronal simulations.

The main contribution of this paper is to demonstrate that, by employing an implicit algorithm and adopting the novel extended magnetic field decomposition strategy proposed herein, we can perform 3D global MHD coronal simulations to evaluate the long-term evolution of coronal structures in practical applications, achieving a computational speed more than 80 times faster than the real-time evolution using only 192 CPU cores. By these means, the time-evolving MHD coronal model, driven by a series of time-evolving magnetograms, can robustly and efficiently resolve low-β issues. Retaining more critical time-evolving information than commonly used quasi-steady-state coronal models do further enables it to capture the dynamic features of the corona with higher fidelity, offering the potential for more accurate simulations of solar disturbances, such as CME propagation.

We employed the thermodynamic time-evolving MHD coronal model, incorporating the extended magnetic field decomposition strategy, to simulate the evolution of the global corona from the solar surface to 20 R_s during two solar maximum CRs within an inertial coordinate system. Completing the 1300 hr evolution of the corona within just 16 hr of computational time validated its efficiency. Given that the maximum magnetic field strength near the solar surface occasionally exceeds 40 G and the plasma β reaches a minimum of approximately 10^{-3}, the model demonstrated

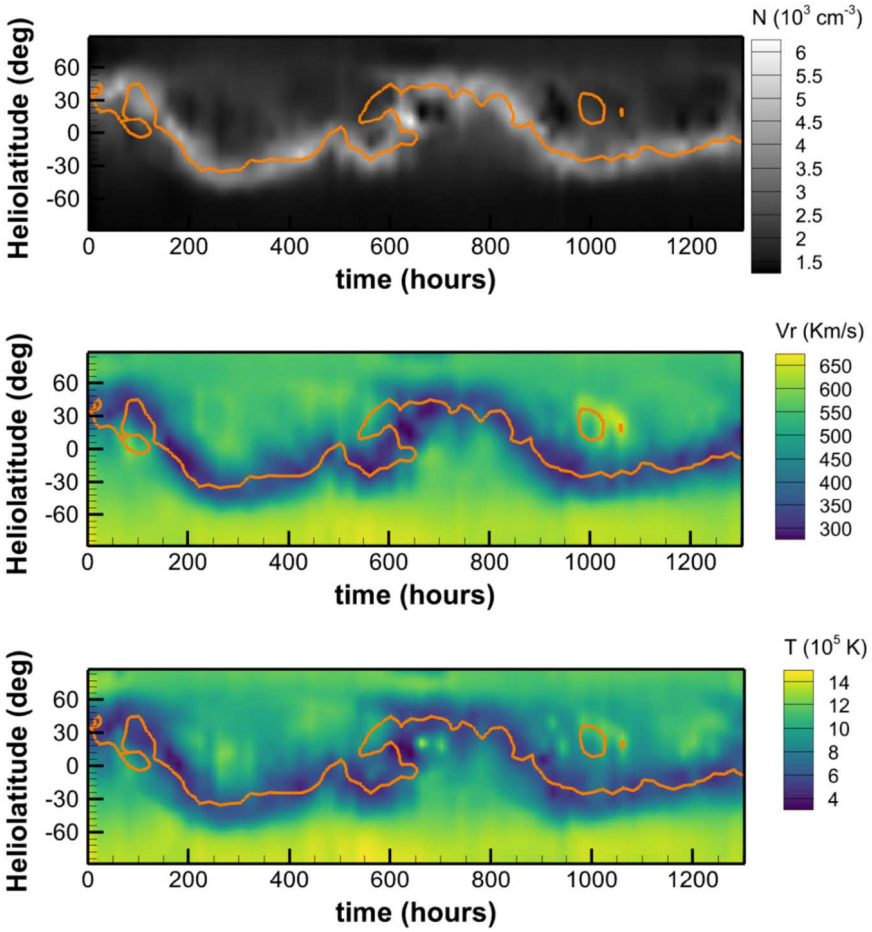

Figure 8. Timing diagrams of simulated plasma number density (10^3 cm^{-3}, top), radial velocity V_r (km s^{-1}, middle) and temperature (10^5 K, bottom) at 20 R_s, corresponding to the same longitude as in Figure 7.

sufficient numerical stability for most solar–terrestrial simulation requirements. Furthermore, the results of the time-evolving simulation basically reproduced remote EUV and pB observations and captured in situ measurements mapped from 1 au to 20 R_s, demonstrating its capability to simulate complex time-evolving coronal structures during solar maximum.

Given that the computational time for simulating 1300 hr of physical time is no more than 16 hr using 192 CPU cores, it is practical to conduct faster-than-real-time CME simulations from the solar surface to 1 au based on this work. We will refine the mesh and extend the coronal model to 1 au, establishing a 3D implicit time-evolving MHD Sun-to-Earth model chain. Additionally, we will use an observation-based flux rope to trigger a realistic CME event in the time-evolving solar–terrestrial MHD model, validating this new generation of CME simulations. Furthermore, this model will be used to enhance and streamline the daily Sun-to-Earth forecasting process and to investigate the dynamic interaction between the solar wind and the magnetosphere of planets such as Jupiter and Saturn.

Although this fully implicit time-evolving MHD solar coronal model, integrated with the extended magnetic field decomposition strategy, offers significant advantages and is a promising tool for timely and accurate simulations of the time-evolving corona in practical space weather forecasting, there is still considerable room for further improvement. Synchronized magnetograms (L. Upton & D. H. Hathaway 2014; J. Linker et al. 2024) are needed to address the limitation of current synoptic magnetographs, where magnetic fields at different longitudes are observed at different times, and to improve the accuracy of reproducing inner-boundary magnetic field when active regions suddenly emerge on the Sun's farside. More accurate measurements of the photospheric magnetic fields in the polar regions are required to reproduce more realistic coronal structures. Additionally, incorporating more physically consistent heating source terms is necessary to better simulate coronal heating and solar wind acceleration during time-evolving simulations. Moreover, self-consistently simulating the formation and evolution of coronal eruptions is crucial for enhancing the reliability of space weather forecasting using numerical models.

In our future work, we plan to incorporate surface flux transport models, such as the advective flux transport model (L. Upton & D. H. Hathaway 2014), along with Solar Orbiter Polarimetric and Helioseismic Imager data (P. Loeschl et al. 2024), horizontal velocities inferred from observational data using the time–distance helioseismology method (J. Zhao et al. 2012; M. S. Yalim et al. 2017), and artificial intelligence-generated data from STEREO EUV observations (H.-J. Jeong et al. 2020, 2022), to advect the radial magnetic field with observed flows and generate a more realistic real-time magnetic field evolution at the inner boundary of our coronal model. Additionally, some models of local active regions (e.g.,

C. W. Jiang et al. 2016; T. Amari et al. 2018; Z. Zhong et al. 2021) will be integrated into this global MHD coronal model to generate energized fields corresponding to transient eruption events. Furthermore, we plan to investigate the wave turbulence-driven heating mechanism (S. R. Cranmer 2010; S. Schleich et al. 2023; Y. H. Gao et al. 2024) in our time-evolving coronal model to gain a better understanding of how both fast and slow solar wind streams are heated and accelerated.

Acknowledgments

This project has received funding from the European Research Council Executive Agency (ERCEA) under the ERC-AdG agreement No. 101141362 (Open SESAME). These results were also obtained in the framework of the projects FA9550-18-1-0093 (AFOSR), C16/24/010 (C1 project Internal Funds KU Leuven), G0B5823N and G002523N (WEAVE) (FWO-Vlaanderen), and 4000145223 (SIDC Data Exploitation (SIDEX), ESA Prodex). This work also benefits from the National Natural Science Foundation of China (grant Nos. 42030204, 42204155, 42274213, and 42474216), and the Specialized Research Fund for State Key Laboratories managed by the Chinese State Key Laboratory of Space Weather. The resources and services used in this work were provided by the Flemish Supercomputer Centre (VSC), funded by the Research Foundation–Flanders (FWO) and the Flemish Government. This work utilizes data obtained by the Global Oscillation Network Group (GONG) program, managed by the National Solar Observatory and operated by AURA, Inc., under a cooperative agreement with the National Science Foundation. The data were acquired by instruments operated by the Big Bear Solar Observatory, High Altitude Observatory, Learmonth Solar Observatory, Udaipur Solar Observatory, Instituto de Astrofísica de Canarias, and Cerro Tololo Inter-American Observatory. The authors also acknowledge the use of the STEREO/SECCHI data produced by a consortium of the NRL (US), LMSAL (US), NASA/GSFC (US), RAL (UK), UBHAM (UK), MPS (Germany), CSL (Belgium), IOTA (France), and IAS (France). This research is (partially) funded by the BK21 FOUR program of Graduate School, Kyung Hee University (GS-1-JO-NON-20242364). E.H. is grateful to the Space Weather Awareness Training Network (SWATNet) funded by the European Union's Horizon 2020 research and innovation program under the Marie Skłodowska-Curie grant agreement No. 955620. Y.Z. acknowledges funding from Research Foundation–Flanders FWO under project No. 1256423N.

ORCID iDs

Haopeng Wang https://orcid.org/0000-0002-4217-6990
Liping Yang https://orcid.org/0000-0003-4716-2958
Stefaan Poedts https://orcid.org/0000-0002-1743-0651
Andrea Lani https://orcid.org/0000-0003-4017-215X
Yuhao Zhou https://orcid.org/0000-0002-4391-393X
Yuhang Gao https://orcid.org/0000-0002-6641-8034
Luis Linan https://orcid.org/0000-0002-4014-1815
Tinatin Baratashvili https://orcid.org/0000-0002-1986-4496
Jinhan Guo https://orcid.org/0000-0002-4205-5566
Rong Lin https://orcid.org/0000-0001-7655-5000
Man Zhang https://orcid.org/0000-0003-3000-2819
Wenwen Wei https://orcid.org/0000-0001-8495-9179
Yun Yang https://orcid.org/0009-0000-5292-713X
Edin Husidic https://orcid.org/0000-0002-1349-3663
Hyun-Jin Jeong https://orcid.org/0000-0003-4616-947X
Mahdi Najafi-Ziyazi https://orcid.org/0009-0008-0922-3995
Brigitte Schmieder https://orcid.org/0000-0003-3364-9183

References

Amari, T., Canou, A., Aly, J.-J., Delyon, F., & Alauzet, F. 2018, Natur, 554, 211
Arge, C. N., Odstrcil, D., Pizzo, V. J., & Mayer, L. R. 2003, in AIP Conf. Proc. 679, Solar Wind Ten (Melville, NY: AIP), 190
Baker, D. N. 1998, AdSpR, 22, 7
Bourdin, P.-A. 2017, ApJL, 850, L29
Brchnelova, M., Kuźma, B., Perri, B., Lani, A., & Poedts, S. 2022, ApJS, 263, 18
Brchnelova, M., Kuźma, B., Zhang, F., et al. 2023, SunGe, 15, 59
Brueckner, G. E., Howard, R. A., Koomen, M. J., et al. 1995, SoPh, 162, 357
Cash, M. D., Biesecker, D. A., Pizzo, V., et al. 2015, SpWea, 13, 611
Cranmer, S. R. 2010, ApJ, 710, 676
Dere, K. P., Del Zanna, G., Young, P. R., & Landi, E. 2023, ApJS, 268, 52
Dere, K. P., Landi, E., Mason, B. C., Monsignori, F., & Young, P. R. 1997, A&AS, 125, 149
Detman, T., Smith, Z., Dryer, M., et al. 2006, JGRA, 111, A07102
Einfeldt, B., Munz, C. D., Roe, P. L., & Sjogreen, B. 1991, JCoPh, 92, 273
Elliott, H. A., Henney, C. J., McComas, D. J., Smith, C. W., & Vasquez, B. J. 2012, JGRA, 117, A09102
Endeve, E., Leer, E., & Holzer, T. E. 2003, ApJ, 589, 1040
Feng, X. S. 2020, Magnetohydrodynamic Modeling of the Solar Corona and Heliosphere (Singapore: Springer)
Feng, X. S., Li, C. X., Xiang, C. Q., et al. 2017, ApJS, 233, 10
Feng, X. S., Liu, X. J., Xiang, C. Q., Li, H. C., & Wei, F. S. 2019, ApJ, 871, 226
Feng, X. S., Lv, J. K., Xiang, C. Q., & Jiang, C. W. 2023, MNRAS, 519, 6297
Feng, X. S., Ma, X. P., & Xiang, C. Q. 2015, JGRA, 120, 10,159
Feng, X. S., Wang, H. P., Xiang, C. Q., et al. 2013, Sci. Sin-Terrae, 43, 912
Feng, X. S., Wang, H. P., Xiang, C. Q., et al. 2021, ApJS, 257, 34
Feng, X. S., Xiang, C. Q., & Zhong, D. K. 2011, Sci. Sin-Terrae, 41, 1
Feng, X. S., Yang, L. P., Xiang, C. Q., et al. 2010, ApJ, 723, 300
Fuchs, F. G., McMurry, A. D., Mishra, S., Risebro, N. H., & Waagan, K. 2010, JCoPh, 229, 4033
Gao, Y. H., Van Doorsselaere, T., Tian, H., Guo, M. Z., & Karampelas, K. 2024, A&A, 689, A195
Gary, G. A. 2001, SoPh, 203, 71
Godunov, S. K. 1959, Matematičeskij Sbornik, 47, 271, https://hal.science/hal-01620642
Griton, L. 2018, PhD Thesis, Université de recherche Paris Sciences et Lettres https://hal.science/tel-01906490v1/file/These_Lea_Griton_2018.pdf
Groth, C. P. T., De Zeeuw, D. L., Gombosi, T. I., & Powell, K. G. 2000, JGR, 105, 25053
Guo, J. H., Linan, L., Poedts, S., et al. 2023, A&A, 683, A54
Guo, X. C. 2015, JCoPh, 290, 352
Hamada, A., Asikainen, T., Virtanen, I., & Mursula, K. 2018, SoPh, 293, 71
Hayashi, K. 2012, JGRA, 117, A08105
Hayashi, K., Abbett, W. P., Cheung, M. C. M., & Fisher, G. H. 2021, ApJS, 254, 1
Hollweg, J. V. 1978, RvGeo, 16, 689
Howard, R. A., Moses, J. D., Vourlidas, A., et al. 2008, SSRv, 136, 67
Jeong, H.-J., Moon, Y.-J., Park, E., & Lee, H. 2020, ApJL, 903, L25
Jeong, H.-J., Moon, Y.-J., Park, E., Lee, H., & Baek, J.-H. 2022, ApJS, 262, 50
Jiang, C. W., Wu, S. T., Feng, X. S., & Hu, Q. 2016, NatCo, 7, 11522
Kimpe, D., Lani, A., Quintino, T., Poedts, S., & Vandewalle, S. 2005, in Proc. 12th European Parallel Virtual Machine and Message Passing Interface Conf., ed. D. K. B. Di Martino & J. J. Dongarra (Berlin: Springer), 520
King, J. H., & Papitashvili, N. E. 2005, JGRA, 110, A02104
Koskinen, H. E. J., Baker, D. N., Balogh, A., et al. 2017, SSRv, 212, 1137
Kuźma, B., Brchnelova, M., Perri, B., et al. 2023, ApJ, 942, 31
Lani, A., Quintino, T., Kimpe, D., et al. 2005, in Computational Science – ICCS 2005, ed. V. S. Sunderan et al. (Berlin: Springer), 281
Lani, A., Villedieu, N., Bensassi, K., et al. 2013, in 21st AIAA Computational Fluid Dynamics Conf. (Reston, VA: American Institute of Aeronautics and Astronautics) AIAA 2013–2589
Lemen, J. R., Title, A. M., Akin, D. J., et al. 2012, SoPh, 275, 17
Li, C. X., Feng, X. S., Xiang, C. Q., et al. 2018, ApJ, 867, 42

Linan, L., Regnault, F., Perri, B., et al. 2023, A&A, 675, A101
Linker, J., Downs, C., Caplan, R., et al. 2024, in EGU General Assembly 2024 (Munich: European Geosciences Union) EGU24–4200
Lionello, R., Downs, C., Mason, E. I., et al. 2023, ApJ, 959, 77
Lionello, R., Linker, J. A., & Mikić, Z. 2008, ApJ, 690, 902
Loeschl, P., Valori, G., Hirzberger, J., et al. 2024, A&A, 681, A59
Mikić, Z., Linker, J. A., Schnack, D. D., Lionello, R., & Tarditi, A. 1999, PhPl, 6, 2217
Owens, M. J., Lockwood, M., & Riley, P. 2017, NatSR, 7, 41548
Parker, E. N. 1963, Interplanetary Dynamical Processes (New York: Interscience)
Perri, B., Brun, A. S., Réville, V., & Strugarek, A. 2018, JPlPh, 84, 765840501
Perri, B., Kuźma, B., Brchnelova, M., et al. 2023, ApJ, 943, 124
Perri, B., Leitner, P., Brchnelova, M., et al. 2022, ApJ, 936, 19
Pesnell, W. D., Thompson, B. J., & Chamberlin, P. C. 2012, SoPh, 275, 3
Petrie, G. J. D., Canou, A., & Amari, T. 2011, SoPh, 274, 163
Pinto, R. F., & Rouillard, A. P. 2017, ApJ, 838, 89
Poedts, S., Lani, A., Scolini, C., et al. 2020, JSWSC, 10, 57
Pomoell, J., & Poedts, S. 2018, JSWSC, 8, A35
Powell, K. G., Roe, P. L., Linde, T. J., Gombosi, T. I., & de Zeeuw, D. L. 1999, JCoPh, 154, 284
Reale, F. 2014, LRSP, 11, 4
Reiss, M. A., Muglach, K., Mason, E., et al. 2024, ApJS, 271, 6
Réville, V., Velli, M., Panasenco, O., et al. 2020, ApJS, 246, 24
Rosner, R., Tucker, W., & Vaiana, G. 1978, ApJ, 220, 643
Samara, E., Pinto, R. F., Magdaleni, J., et al. 2021, A&A, 648, A35
Schleich, S., Boro Saikia, S., Ziegler, U., Güdel, M., & Bartel, M. 2023, A&A, 672, A64
Tanaka, T. 1995, JGRA, 100, 12057
Upton, L., & Hathaway, D. H. 2014, ApJ, 780, 5
van der Holst, B., Sokolov, I. V., Meng, X., et al. 2014, ApJ, 782, 81
Wang, H. P., Guo, J. H., Yang, L. P., et al. 2025a, A&A, 693, A257
Wang, H. P., Poedts, S., Lani, A., et al. 2025b, A&A, 694, A234
Wang, H. P., Xiang, C. Q., Liu, X. J., Lv, J. K., & Shen, F. 2022a, ApJ, 935, 46
Wang, H. P., Zhao, J. M., Lv, J. K., & Liu, X. J. 2022b, Chin. J. Geophys., 65, 2779
Wang, Y., Feng, X. S., & Xiang, C. Q. 2019, CF, 179, 67
Wang, Y. M. N. R., Sheeley, J., & Rich, N. B. 2007, ApJ, 658, 1340
Wu, K. L., & Shu, C. W. 2019, NuMat, 142, 995
Xia, C., Chen, P. F., Keppens, R., & van Marle, A. J. 2011, ApJ, 737, 27
Xia, C., Teunissen, J., Mellah, I. E., Chané, E., & Keppens, R. 2018, ApJS, 234, 30
Yalim, M. S., Pogorelov, N., & Liu, Y. 2017, JPhCS, 837, 012015
Yang, L. P., Feng, X. S., Xiang, C. Q., et al. 2012, JGRA, 117, A08110
Yeates, A., Amari, T., Contopoulos, I., et al. 2018, SSRv, 214, 99
Zhao, J., Couvidat, S., Bogart, R. S., et al. 2012, SoPh, 275, 375
Zhong, Z., Guo, Y., & Ding, M. 2021, NatCo, 12, 2734
Zhou, Y. H., Ruan, W. Z., Xia, C., & Keppens, R. 2021, A&A, 648, A29